

Semi-inclusive direct photon+jet and π^0 +jet correlations measured in $p + p$ and central Au + Au collisions at $\sqrt{s_{\text{NN}}} = 200$ GeV

The STAR Collaboration

September 18, 2023

Abstract

The STAR experiment at RHIC reports new measurements of jet quenching based on the semi-inclusive distribution of charged-particle jets recoiling from direct photon (γ_{dir}) and neutral pion (π^0) triggers in $p + p$ and central Au+Au collisions at $\sqrt{s_{\text{NN}}} = 200$ GeV, for triggers in the range $9 < E_{\text{T}}^{\text{trig}} < 20$ GeV. The datasets have integrated luminosities of 3.9 nb^{-1} for Au + Au and 23 pb^{-1} for $p + p$ collisions. Jets are reconstructed using the anti- k_{T} algorithm with resolution parameters $R = 0.2$ and 0.5 . The large uncorrelated jet background in central Au + Au collisions is corrected using a mixed-event approach, which enables precise charged-particle jet measurements at low transverse momentum $p_{\text{T,jet}}^{\text{ch}}$ and large R . Recoil-jet distributions are reported in the range $p_{\text{T,jet}}^{\text{ch}} < 25$ GeV/ c . Comparison of the distributions measured in $p + p$ and Au + Au collisions reveals strong medium-induced jet yield suppression for $R = 0.2$, with markedly less suppression for $R = 0.5$. These data provide new insight into the mechanisms underlying jet quenching, and the angular dependence of medium-induced jet-energy transport.

1 Introduction

Matter under conditions of extreme temperature and density comprises a Quark-Gluon Plasma (QGP), the state of matter in which the predominant

degrees of freedom are sub-hadronic [1, 2]. QGP filled the universe a few microseconds after the Big Bang, and is generated and studied today in collisions of heavy atomic nuclei at the Relativistic Heavy Ion Collider (RHIC) and the Large Hadron Collider (LHC). Measurements at these facilities, and their comparison to theoretical calculations, show that the QGP is a fluid with very low specific viscosity [3–6] that is opaque to the passage of energetic color charges [7].

Jets provide unique and incisive probes of the QGP. In hadronic collisions, jets are generated by hard (high momentum transfer Q^2) interactions of incoming quarks and gluons (partons). The scattered partons are initially highly virtual, and evolve by radiating gluons to produce a collimated parton shower. Quantum interference in this radiative process produces distinctive features, notably angular ordering, whereby the most energetic jet fragments are most closely aligned with the jet axis. Jet reconstruction algorithms have been developed that can be applied to both experimental data and to theoretical calculations based on perturbative Quantum Chromodynamics (pQCD) [8]. Using these algorithms, pQCD calculations are found to be in excellent agreement with jet measurements at hadron colliders [9–14].

In nuclear collisions at RHIC and the LHC, jets are generated in coincidence with the nascent QGP. Highly-virtual partons from hard scatterings interact with the colored constituents of the QGP, scattering elastically and radiatively [7, 15]. These in-medium interactions modify jet production rates and properties relative to those of jets generated in vacuum, producing several experimentally observable effects (“jet quenching”) [16–19]: jet energy loss due to transport of energy out of the jet cone, corresponding to yield suppression at fixed transverse momentum (p_T); modification of intra-jet structure; and deflection of the jet centroid (acoplanarity).

Measurements of reconstructed jets in heavy-ion collisions are challenging, due to the large and complex background from uncorrelated processes (see Ref. [7] and references therein). Jet quenching was initially observed in measurements of inclusive production and correlations of high- p_T hadrons, the leading fragments of jets, which are more readily measurable over the large background in heavy-ion collisions [20–32]. The comparison of high- p_T hadron yield suppression measurements with theoretical calculations provides significant constraints on the QGP transport parameter \hat{q} , which characterizes the momentum exchange of jets with the QGP medium due to interactions [33–35]. High- p_T hadrons are sensitive primarily to the magnitude of in-medium jet energy loss, however, and more detailed understanding of

the mechanisms underlying jet quenching requires measurements based on reconstructed jets [12, 36–50].

An important channel for such measurements is the coincidence of an isolated direct photon (γ_{dir}) and recoiling jet [51]. Direct photons are colorless and do not interact significantly with the QGP; their transverse energy (E_{T}) thereby provides a reference scale for precise measurements of jet quenching [52]. In the theoretical description of γ_{dir} +jet pair production at RHIC energies, at leading perturbative order (LO) the predominant mechanism is QCD Compton scattering ($qq \rightarrow \gamma q$), in which the direct photon E_{T} and recoiling quark jet p_{T} are balanced [52]. However, Next-to-Leading Order (NLO) contributions, which generate photon-jet p_{T} -imbalance, are sizable even in vacuum [53]. Measurement of the γ_{dir} +jet channel is nevertheless a key element of the program for precise jet quenching measurements at RHIC and the LHC.

Coincidence γ_{dir} +jet measurements have been carried out for $p + p$ and Pb + Pb collisions at the LHC [43, 54, 55]. The $p + p$ measurements exhibit significant p_{T} imbalance, consistent with NLO calculations [53], while jet quenching is found to generate additional p_{T} imbalance that is however smaller in magnitude than in-vacuum NLO effects [54, 55]. There are currently no γ_{dir} +jet measurements reported at RHIC.

Measurements of the semi-inclusive distribution of jets recoiling from a high- p_{T} hadron trigger have been carried out for $p + p$, Pb + Pb and p + Pb collisions at the LHC [40, 56], and for Au + Au collisions at RHIC [49]. In the semi-inclusive approach, selection bias is induced solely by the choice of trigger. Due to the effects of jet quenching, observed high- p_{T} hadrons in nuclear collisions are generated predominantly at the surface of the QGP, headed outwards [57]; for semi-inclusive observables with a hadron trigger, the recoiling jet population may therefore have on average larger in-medium path length than an unbiased population [40, 49]. Semi-inclusive measurements incorporating both γ_{dir} and π^0 triggers can provide direct comparison of recoil-jet populations with different quark/gluon relative populations and different in-medium path-length distributions [58].

This manuscript and the companion Letter [59] report the first γ_{dir} +jet and π^0 +jet coincidence measurements in $p + p$ and central Au + Au collisions at $\sqrt{s_{\text{NN}}} = 200$ GeV. Semi-inclusive distributions of charged-particle jets [40, 49] recoiling from identified γ_{dir} and π^0 trigger particles are reported, for triggers in the range $9 < E_{\text{T}}^{\text{trig}} < 20$ GeV. The analysis is based on previous developments to discriminate γ_{dir} and π^0 at high p_{T} by using calorimetric

shower shape [58, 60], and to mitigate the complex jet background in central Au + Au collisions by means of mixed events (ME) [49]. This manuscript presents the analysis and experimental results in detail, while the companion Letter compares the measurements to theoretical calculations and discusses the constraints that these measurements impose on the physical mechanisms underlying jet quenching.

Jets are reconstructed using the anti- k_T algorithm [61] with resolution parameters $R = 0.2$ and 0.5 . In-medium jet energy loss is measured by comparing $p_{T,\text{jet}}$ distributions in Au + Au and $p + p$ collisions at the same R , and intra-jet broadening is measured by comparing the distributions at different R in Au + Au and $p + p$ collisions separately. This manuscript and the companion Letter focus on recoil-jet yield distributions as a function of $p_{T,\text{jet}}$; more differential measurements of the angular distribution of recoil jets will be reported in a forthcoming publication.

The manuscript is organized as follows: Sect. 2 presents the detector, dataset, and offline reconstruction; Sect. 3 presents the theoretical model calculations that are compared to data; Sect. 4 presents an overview of the analysis; Sect. 5 presents the photon and π^0 measurements; Sect. 6 presents the jet reconstruction; Sect. 7 presents the raw coincidence distributions; Sect. 8 presents the extraction of $\gamma_{\text{dir}}+\text{jet}$ distributions; Sect. 9 presents trigger-resolution effects; Sect. 10 presents corrections to the recoil $p_{T,\text{jet}}$ distributions; Sect. 11 presents systematic uncertainties; Sect. 12 presents closure tests; Sect. 13 presents the physics results; and Sect. 14 presents a summary and outlook.

2 Dataset, offline analysis, and simulations

The Solenoidal Tracker at RHIC (STAR) detector is described in Ref. [62]. STAR has a large solenoidal magnet with uniform magnetic field of strength of 0.5 T aligned with the beam direction, and detectors for triggering, tracking, electromagnetic calorimetry, and particle identification. This analysis utilizes the Barrel Electromagnetic Calorimeter (BEMC) [63] for triggering and EM shower measurements; the Barrel Shower Maximum Detector (BSMD) [58] for γ/π^0 discrimination; the Time Projection Chamber (TPC) [64] for charged-particle tracking; and the forward Vertex Position Detector (VPD) and Zero-Degree Calorimeter (ZDC) for triggering. The BEMC, BSMD, and TPC have acceptance in pseudo-rapidity $|\eta| < 1.0$, with

full azimuthal coverage.

The data for $p + p$ collisions at $\sqrt{s} = 200$ GeV were recorded during the high luminosity phase of the 2009 RHIC run. The data were selected online using the L2Gamma trigger. The first layer of event selection, after receiving data from the detectors, passes the event to the L2Gamma trigger based on the presence of at least one BEMC “high tower” with transverse energy E_T greater than 4.2 GeV. The L2Gamma selection requires the presence of a contiguous cluster of 3×3 BEMC towers, whose two most energetic towers have sum $E_T > 7.44$ GeV. In total, 11.3 million $p + p$ collision events were recorded which satisfy the L2Gamma trigger requirements. After offline cuts for event quality, the $p + p$ integrated luminosity accepted for analysis is 23 pb^{-1} .

The data for Au + Au collisions at $\sqrt{s_{NN}} = 200$ GeV were recorded during the 2014 RHIC run, likewise utilizing the L2Gamma selection. In this case, the first layer of triggering is a high-tower E_T threshold of 5.9 GeV. No centrality-specific selection is applied at the online trigger level. Pileup is suppressed offline by comparing two different measurements of the event-vertex position along the beam direction: reconstructed using tracks (see below), and measured by VPD timing. Events are rejected if the difference between the vertex-position measurements is greater than 6 cm along the beam direction, or if the track-based vertex position has distance larger than 70 cm from the nominal center of STAR in the beam direction. Since the Time-of-Flight (TOF) detector has faster readout than the TPC, the fraction of TPC tracks matched to TOF hits is also used to reject uncorrelated events. Additionally, events with noisy trigger towers, defined as those having a hit frequency greater than 5σ from the average of all towers, are rejected. After offline cuts for event quality, the integrated luminosity for Au + Au collisions accepted for the analysis is 3.9 nb^{-1} .

Charged-particle tracks are reconstructed offline using hits in the TPC. Global tracks are defined as charged-particle tracks having at least 5 out of the maximum 45 hits possible in the TPC. Primary tracks are a subset of the global tracks, having distance of closest approach to the primary vertex less than 3 cm. The primary vertex position in the beam direction, denoted z_{vtx} , is determined as the average position of these tracks extrapolated to the beamline. The primary vertex is then included in the momentum fit for primary tracks.

For Au + Au collisions, centrality is determined using the multiplicity of global tracks that have at least 10 hits in the TPC; a distance of closest

approach to the primary vertex less than 3 cm; and $|\eta_{\text{track}}| < 0.5$. The luminosity dependence of the centrality determination is accounted for, using the average instantaneous coincidence rate in the ZDCs. The variation in acceptance with vertex position is corrected by weighting to the charged-track multiplicity distribution, to render the average charged-track multiplicity uniform as a function of z_{vtx} . In this analysis, “central Au + Au collisions” refers to the event population with multiplicity in the highest 15% interval of the multiplicity distribution for all Au + Au hadronic interactions.

Jet reconstruction uses primary tracks. The primary track acceptance is $|\eta_{\text{track}}| < 1.0$ and $0.2 < p_{\text{T,track}} < 30 \text{ GeV}/c$, over the full azimuth. Additional primary-track selection criteria require the track to have more than 15 TPC hits, and the ratio of the number of its measured hits over the maximum possible (depending upon track geometry) to be greater than 52%. The primary-track yield with $p_{\text{T,track}} > 30 \text{ GeV}/c$ is negligible for both collision systems. The primary-track efficiency is 60% at $p_{\text{T,track}} = 0.5 \text{ GeV}/c$ and 72% for $p_{\text{T,track}} > 2 \text{ GeV}/c$ in central Au + Au collisions, and 82% for $p_{\text{T,track}} > 1 \text{ GeV}/c$ in $p + p$ collisions (see Ref. [65] for details). The primary-track momentum resolution is approximately $\sigma_{p_{\text{T}}}/p_{\text{T}} = 0.01 \cdot p_{\text{T}} [\text{GeV}/c]$, for both central Au + Au and $p + p$ collisions.

Detector simulations are carried out using GEANT3 [66] with a detailed model of the STAR detector. Simulations based on the PYTHIA Monte Carlo event generator are used both to calculate the instrumental response to correct for detector effects and for physics studies. Events produced by Monte Carlo generation without detector simulations are denoted “particle-level,” whereas such events including detector simulations are denoted “detector-level.”

Several PYTHIA tunes are employed: PYTHIA-6 [67] Perugia 0 [68]; PYTHIA-6 Perugia 2012 STAR tune [69]; and PYTHIA-8 Monash [70]. The reason for using multiple PYTHIA tunes is historical, since different elements of the analysis, such as detector-level simulations, were carried out at different times by different sub-groups. The tune used for each analysis element is specified. Physics studies focus on comparison to PYTHIA-6 Perugia 2012 STAR tune (denoted “PYTHIA-6 STAR tune”).

3 Theoretical calculations

In the companion Letter [59], results are compared to the following theoretical calculations that incorporate jet interactions with the QGP:

- Jet-fluid model [72]: Initial conditions and the jet shower evolution are generated by PYTHIA. The QGP is modeled using 2+1 dimensional VISHNU hydrodynamics [73]. Jet propagation takes into account both elastic and inelastic energy loss, with latter calculated using the Higher Twist (HT) formalism, as well as p_T -broadening. Only the jet shower is modified; jet-induced medium excitation (“back-reaction”) is not considered.
- Linear Boltzmann Transport (LBT) model [74]: Jet generation and shower evolution are calculated using PYTHIA. The QGP is modeled using CLVisc 3+1 dimensional viscous hydrodynamics [75] with AMPT initial conditions [76]. Jet propagation in the QGP includes both elastic and inelastic processes, with the latter calculated using the HT formalism. Back-reaction to the QGP medium arises from rescattering of thermal recoil partons with jet shower partons. The linear approximation corresponds to such rescatterings only occurring between jet and thermal medium partons. Energy and momentum are explicitly conserved.
- Coupled Linear Boltzmann Transport and hydro (CoLBT-hydro) model [77, 78]: modifies the LBT model by including jet-induced medium excitation in the hydrodynamic evolution, thereby relaxing the linear approximation. This extends the applicability of the model to the case in which the medium excitation is similar in magnitude to the local thermal parton density.
- Soft Collinear Effective Theory (SCET) model [53, 79]: Photon-jet distributions are calculated using PYTHIA. The QGP has initial energy density proportional on average to participant number density, with event-by-event fluctuations, and evolves according to 2+1 dimensional viscous hydrodynamics. Jet-medium inelastic interactions are calculated using the GLV approach at first order in opacity, with a soft gluon emission approximation. Elastic interactions are also included. Energy loss is controlled by a variable coupling strength, with relative

energy loss of quarks and gluons proportional to their color charges. Excitation of the QGP medium is equated with the jet energy transported beyond the jet cone radius R .

- Hybrid model [80, 81]. Hard processes are generated by PYTHIA, with the jet shower evolved by PYTHIA down to a cutoff virtuality $Q_0 = 1$ GeV. The jet showers are embedded in a hydrodynamically expanding medium and interact with it non-pertubatively, using a holographic expression for energy loss derived from gauge/gravity duality. Energy and momentum lost by the interacting jet are absorbed by the QGP, manifesting as a wake of soft particles surrounding the jet. Generation of the wake can optionally be switched off.

4 Analysis overview

STAR has previously reported measurements of $\gamma_{\text{dir}} + \text{hadron}$ and $\pi^0 + \text{hadron}$ coincidence distributions in $p + p$ and Au + Au collisions [58, 60], and semi-inclusive distributions of charged-particle jets recoiling from high- p_T charged-hadron triggers in Au + Au collisions [49], both at $\sqrt{s_{\text{NN}}} = 200$ GeV. These analyses required the development of new procedures to enable systematically well-controlled measurements in the large-background environment of central Au + Au collisions.

The analysis reported here combines these new approaches to measure semi-inclusive distributions of charged-particle jets recoiling from high- p_T γ_{dir} and π^0 triggers in $p + p$ and Au + Au collisions at $\sqrt{s_{\text{NN}}} = 200$ GeV. While we follow closely the procedures in Refs. [49, 58], this analysis utilizes different datasets, and its performance and systematic uncertainties must therefore be evaluated in full. This section presents an overview of the analysis strategy and approach, with details provided in subsequent sections.

4.1 Semi-inclusive distributions

Jet measurements in the high-multiplicity environment of a heavy-ion collision are complex, due to the large uncorrelated background. Reconstructed jets in this environment therefore can have contributions from physical jets generated by the hard process of interest (inclusive or triggered-coincidence production); physical jets generated by other hard processes (multiple high-

Q^2 partonic interactions, or MPIs); and a combinatorial component comprising hadrons from soft (low- Q^2) interactions. The analysis must remove the jet yield component that is not correlated with the process of interest (which may not include MPIs, depending upon the application), and then correct the $p_{T,\text{jet}}$ smearing due to the residual uncorrelated contribution [40, 49, 82].

Semi-inclusive measurements enable data-driven procedures for such corrections over broad phase space [40, 49]. In this approach, the event selection and jet measurement are carried out in separate steps. Events are first selected using a simple trigger condition, with the trigger particle distribution sampled inclusively. Jet reconstruction is then carried out on the selected events and the number of jets in a defined recoil acceptance is counted, without any requirements on the jet population beyond acceptance.

The measured semi-inclusive distribution, corresponding to the distribution of recoil jets normalized to the number of trigger particles, is equivalent in the absence of background to the ratio of two production cross sections [40, 49]:

$$\left(\frac{1}{N_{\text{trig}}^{\text{A+A}}} \cdot \frac{dN_{\text{jet}}^{\text{A+A}}}{dp_{T,\text{jet}}^{\text{ch}} d\Delta\varphi} \right) \Bigg|_{p_T^{\text{trig}}} = \left(\frac{1}{\sigma^{\text{A+A} \rightarrow \text{trig}}} \cdot \frac{d\sigma^{\text{A+A} \rightarrow \text{trig+jet}}}{dp_{T,\text{jet}}^{\text{ch}} d\Delta\varphi} \right) \Bigg|_{p_T^{\text{trig}}}, \quad (1)$$

where $p_{T,\text{jet}}^{\text{ch}}$ is the recoil-jet transverse momentum; $\Delta\varphi$ is the azimuthal angular separation between trigger and recoil jet; $\sigma^{\text{A+A} \rightarrow \text{trig}}$ is the inclusive production cross section for the trigger particle; and $\sigma^{\text{A+A} \rightarrow \text{trig+jet}}$ is the production cross section for both trigger and recoil jet in the acceptance. Preferred trigger particles satisfy two criteria: they can be measured precisely in central A + A collisions without complex event-wise background corrections; and the cross sections in Eq. 1 can be calculated perturbatively. Preferred trigger particles are therefore charged hadrons, π^0 , direct photons, and (at the LHC) Z-bosons.

Since jets do not play a role in event selection in the semi-inclusive approach, selection bias is induced solely by the choice of trigger [40, 49]. This analysis employs both γ_{dir} and π^0 triggers, whose event-selection biases are expected to differ. These differences include:

- **Relative q/g contribution to recoil-jet population:** High- E_T γ_{dir} and high- p_T π^0 are generated by different distributions of partonic scattering processes [83]. Figure 1 shows a calculation illustrating this, using events generated by PYTHIA for $p + p$ collisions at $\sqrt{s} = 200$ GeV.

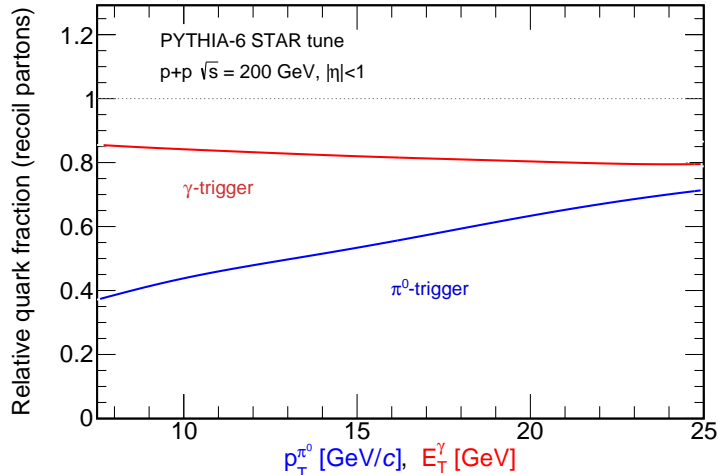


Figure 1: Relative fraction of quarks ($q/(q + g)$) recoiling from a π^0 or γ_{dir} trigger as a function of $p_{\text{T}}^{\text{trig}}$ or $E_{\text{T}}^{\text{trig}}$, calculated using PYTHIA-6 STAR tune for $p + p$ collisions at $\sqrt{s} = 200$ GeV. Acceptance is $|\eta| < 1.0$ for both trigger particle and recoil partons.

Events containing a high- E_{T} γ_{dir} and high- p_{T} π^0 are selected and the relative fraction of quarks in the population of recoil partons is determined.¹ The quark fraction of recoil partons is seen to be significantly larger for γ_{dir} than for π^0 triggers at the same value of $E_{\text{T}}^{\text{trig}}$ or $p_{\text{T}}^{\text{trig}}$, for the range considered in this analysis ($9 < E_{\text{T}}^{\text{trig}} < 20$ GeV, see Sect. 5).

- **In-medium path-length distribution of recoil jets:** Due to the interplay of the inclusive $p_{\text{T,jet}}$ -distribution, π^0 fragmentation function, and energy loss effects, observed high- p_{T} π^0 are expected to arise predominantly from the fragmentation of jets that have experienced little energy loss due to quenching, corresponding predominantly to jets generated at the periphery of the QGP fireball and headed outward [57, 84–86]. In that case, the in-medium path-length distribution of jets recoiling from π^0 triggers is biased towards larger values than

¹This calculation assumes a LO ($2 \rightarrow 2$) production process and identifies the “recoil parton” in each PYTHIA event as the highest-energy parton within the same recoil acceptance as the data analysis. Accounting for additional QCD effects requires theoretical considerations that are beyond the scope of this study.

that of the inclusive jet population [40,49]. Since γ_{dir} do not lose energy due to jet quenching, jets recoiling from γ_{dir} triggers do not have such a path-length bias; their in-medium path-length distribution is the same as that of the inclusive jet population.

- **Event-Plane (EP) orientation:** A correlation between high- p_{T} hadron production and EP orientation (observed second-order plane of symmetry constructed from the soft hadron distribution) has been observed in Au+Au collisions [87]. In this analysis, for π^0 triggers such a correlation could generate a dependence of background yield on the relative orientation of the trigger and EP, and possibly an in-medium path-length bias for the recoiling jet population. The EP-orientation dependence of the recoil spectrum was measured in the previous h +jet analyses, with negligible dependence found for central A + A collisions at both RHIC and the LHC [40,49]. No such dependence is expected for γ_{dir} triggers.

We note that the selection-bias effects we discuss here are expectations based on model calculations. We return to these expectations in Sect. 13, when comparing the measured recoil-jet distributions for γ_{dir} and π^0 triggers.

4.2 Recoil-jet measurement

For events accepted by the trigger selection, jet reconstruction is carried out with charged particles using the anti- k_{T} algorithm [61] with resolution parameters $R = 0.2$ and 0.5 . Detailed discussion of jet reconstruction is presented in Sect. 6. Recoil jets are accepted in $\Delta\varphi \in [3\pi/4, 5\pi/4]$ and $|\eta_{\text{jet}}| < 1.0 - R$, where η_{jet} is the pseudo-rapidity of the jet centroid. Corrections to the two-dimensional distribution, which are a function of $p_{\text{T,jet}}^{\text{ch}}$ and $\Delta\varphi$, are applied to account for uncorrelated jet yield and $p_{\text{T,jet}}$ -smearing due to background. These corrections are carried out separately: first a “vertical” correction to subtract uncorrelated-jet yield, followed by a “horizontal” correction for $p_{\text{T,jet}}$ -smearing of the distribution of correlated yield (Sect. 10).

The goal of the analysis is to measure the recoil-jet yield over broad phase space, including low $p_{\text{T,jet}}$ and large R where the ratio of trigger-correlated signal and uncorrelated background yield (S/B) is small. The correction for uncorrelated yield must be fully data-driven, in order to achieve high systematic precision in the region of small S/B. Since individual hadrons cannot be attributed uniquely to a trigger-correlated recoil jet or to uncor-

related background, such corrections are carried out statistically, i.e. at the level of ensemble-averaged distributions [40, 49].

Two related but distinct statistical approaches have been developed to determine the uncorrelated recoil-jet yield distribution. The ALICE collaboration utilizes two different ranges of p_T^{trig} for this purpose (“Signal” and “Reference”) [40], while the STAR collaboration utilizes a distribution constructed from mixed events in place of the Reference distribution [49]. In both approaches, the raw value of $p_{T,\text{jet}}$ is first shifted by the estimated median level of uncorrelated p_T -density ρ in each event, scaled by the jet area [88]. The resulting distribution, $p_{T,\text{jet}}^{\text{reco, ch}}$, is peaked near $p_{T,\text{jet}}^{\text{reco, ch}} = 0$, with approximately half of all jet candidates having $p_{T,\text{jet}}^{\text{reco, ch}} < 0$ [40, 49] (see Sect. 6).

The Signal and Reference (ALICE) or ME (STAR) distributions in the region of large negative $p_{T,\text{jet}}^{\text{reco, ch}}$ are found to have identical shape to high precision, indicating that this region is strongly dominated by uncorrelated yield [40, 49], and is therefore the optimal region for precise normalization of the Reference or ME distribution. After normalization, the correlated recoil-jet yield distribution is determined by subtraction. This difference distribution is subsequently corrected for smearing in $p_{T,\text{jet}}$ and $\Delta\varphi$ using unfolding techniques. This statistical approach enables systematically well-controlled measurements of recoil-jet yield with small S/B over the entire physically-allowed phase space, without the need to impose a fragmentation bias on the recoil-jet population in order to suppress backgrounds [49].

The ALICE p_T^{trig} -difference and STAR ME approaches to uncorrelated background correction are compared in Ref. [49]. The key distinction between them is that the trigger-difference approach subtracts all uncorrelated recoil yield, including physical jets generated by MPIs, whereas the ME approach does not subtract jets arising from MPIs. This difference was found to have negligible effect for h +jet correlations in central Au+Au collisions at $\sqrt{s_{\text{NN}}} = 200$ GeV [49].

4.3 Observables

The trigger-normalized jet yield in the recoil acceptance is defined as

$$Y(p_{T,\text{jet}}^{\text{ch}}, R) = \frac{1}{N_{\text{trig}}} \int_{3\pi/4}^{5\pi/4} d\Delta\varphi \left[\frac{d^2 N_{\text{jet}}(R)}{dp_{T,\text{jet}}^{\text{ch}} d\Delta\varphi} \right]_{E_T^{\text{trig}} \in [E_T^{\text{min}}, E_T^{\text{max}}]}, \quad (2)$$

where R is the jet reconstruction resolution parameter. The distribution is also differential in jet pseudo-rapidity η_{jet} , which is not specified for clarity. All distributions are normalized to unit interval in η_{jet} . This definition applies for both $p + p$ and Au + Au collisions, and for both raw and fully corrected distributions. The collision system and level of correction are indicated by superscripts, where needed.

Jet energy loss due to jet quenching is measured by the ratio of corrected trigger-normalized jet yields in central Au + Au and $p + p$ collisions,

$$I_{\text{AA}} = \frac{Y^{\text{Au+Au}}(p_{\text{T,jet}}^{\text{ch}}, R)}{Y^{p+p}(p_{\text{T,jet}}^{\text{ch}}, R)}. \quad (3)$$

Measurements of I_{AA} using h +jet correlations have been reported at RHIC and the LHC [40, 49].

The transverse broadening of jet structure due to quenching is measured by the ratio of trigger-normalized recoil-jet yields at small and larger R separately in $p + p$ and Au + Au collisions,

$$\mathfrak{R}_{\text{large-}R}^{\text{small-}R} = \frac{Y^{\text{A+A}}(p_{\text{T,jet}}^{\text{ch}}, \text{small } R)}{Y^{\text{A+A}}(p_{\text{T,jet}}^{\text{ch}}, \text{large } R)}, \quad (4)$$

where A + A refers to either $p + p$ or Au + Au. This ratio is less than unity for inclusive jets in $p + p$ collisions, reflecting jet shapes in vacuum [40, 89–92]. To date, no significant medium-induced transverse broadening has been observed in semi-inclusive measurements [40, 49].

We note that interpretation of the ratio in Eq. 4 in terms of jet broadening requires corresponding jet populations in the numerator and denominator, i.e. jet reconstruction does not split a single jet reconstructed with large R into multiple jets reconstructed with small R at a significant rate. As discussed in Sect. 13.3, that condition may not hold in this analysis for very low- p_{T} jets, for which $p_{\text{T,jet}}^{\text{ch}} \ll p_{\text{T}}^{\text{trig}}$.

5 Measurement of γ and π^0 triggers

The measurement of γ_{dir} and π^0 triggers in this analysis uses the same procedures as in Ref. [58]. Events are selected online using the L2Gamma trigger. Offline analysis further selects events containing electromagnetic showers with $9 < E_{\text{T}}^{\text{trig}} < 20$ GeV measured in one or two adjacent BEMC towers.

This E_T^{trig} range is chosen such that the π^0 -decay opening angle is small enough that the two photons are likely to hit the same tower, but not so small that the transverse shower profile measured in the BSMD is indistinguishable from that for a single photon. The threshold value of $E_T^{\text{trig}} = 9$ GeV is optimal for identifying π^0 triggers, with efficiency significantly lower for $E_T^{\text{trig}} > 20$ GeV. In addition, the threshold value of 9 GeV is large enough that there is significant recoil-jet yield, while also providing sufficient dynamic range for the measurement of three bins in E_T^{trig} .

Discrimination of γ and π^0 showers utilizes the transverse-shower shape measured by the BSMD. Although the opening angle for the two decay photons from a π^0 is small enough that they typically hit the same or neighboring towers, the resulting electromagnetic shower in the BSMD is broader than that of a single photon.

Each BEMC tower subtends $\Delta\eta \times \Delta\phi = 0.05 \times 0.05$, and each set of 15 η and 15 ϕ BSMD strips overlapping a BEMC tower subtends $\Delta\eta \times \Delta\phi = 0.1 \times 0.1$. For the shower-shape analysis, BSMD η and ϕ strips are clustered [58], and clusters whose central strips overlap geometrically with the BEMC trigger tower are identified. The intersection of the central η and ϕ BSMD strips in a cluster, determined by the strip with the largest energy relative to ± 7 adjacent strips in both η and ϕ , localizes the centroid of the shower with spatial resolution of 0.007 radians. The BEMC tower overlapping the centroid is identified as the central tower of the cluster if it also has an energy of at least 6 GeV. If the shower centroid falls within 0.018 radians of the edge of the triggering tower, then the nearest tower is also included in the energy measurement. Charged-particle tracks are projected to the face of the BEMC, and trigger towers that contain the projection of a track with $p_T > 2$ GeV/ c are rejected.

The shower shape is quantified by the Transverse Shower Profile (TSP), defined as $\text{TSP} = E_{\text{tower}} / \sum_i e_i r_i^{1.5}$, where E_{tower} is the BEMC trigger-tower energy; e_i is the energy of the i -th BSMD strip; r_i is the distance between the i -th strip and the center of the cluster, and the sum runs over the 15 strips in η and ϕ which define the BSMD cluster. The value of r_i for the central strip is taken to be half the distance between strips. The value of the exponent, 1.5, was determined by optimizing γ/π^0 discrimination using a GEANT simulation [58].

Figure 2 shows the TSP distribution measured in central Au + Au and $p + p$ collisions. The TSP cut labeled π^0 , corresponding to $\text{TSP} < 0.08$, generates a shower population with π^0 purity greater than 95%. However,

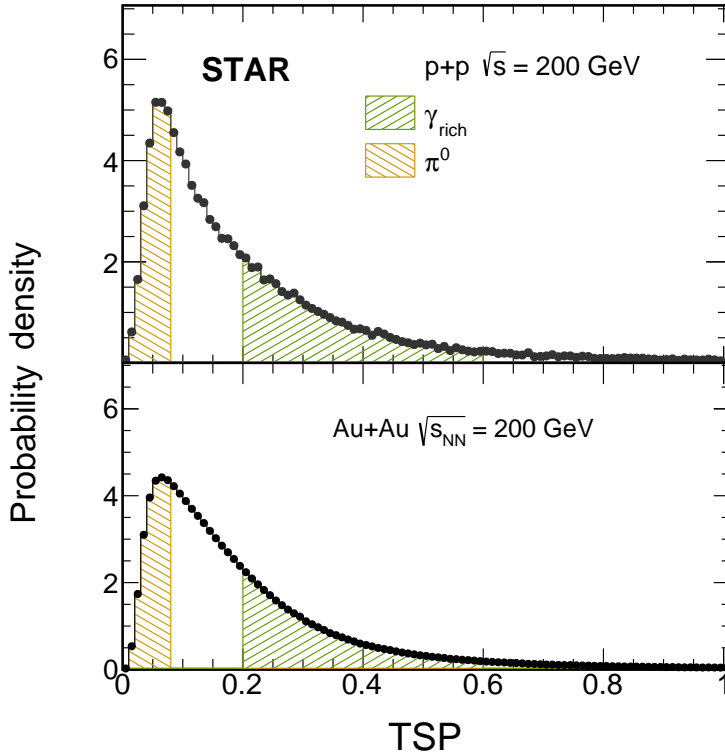


Figure 2: TSP distributions for $p + p$ (upper) and central Au + Au (lower) collisions. The orange and green regions show the selection for the π^0 and γ_{rich} triggers, respectively.

such high purity cannot be achieved for γ_{dir} with a TSP cut. Rather, a γ_{rich} population is selected by $0.2 < \text{TSP} < 0.6$, which contains a significant admixture of π^0 triggers and photons from π^0 and η decays, whose fraction is measured using the relative rate of near-side hadrons (where proximity is determined from the relative azimuthal angle $\Delta\phi$) as a function of $E_{\text{T}}^{\text{trig}}$ (Sect. 8).

Based on these TSP cuts, the central Au + Au dataset contains about 56000 π^0 and 134000 γ_{rich} triggers, while the $p + p$ dataset contains about 18000 π^0 and 24000 γ_{rich} triggers. These trigger populations are then divided into bins with $E_{\text{T}}^{\text{trig}}$ in the ranges [9,11], [11,15] and [15,20] GeV. The number

of triggers in each E_T^{trig} bin is shown in Tab. 1.

Table 1: Number of events containing a trigger passing all event- and trigger-selection criteria for π^0 and γ_{rich} selections, for the E_T^{trig} bins used in the analysis.

$E_T^{\text{trig}}[\text{GeV}]$	$p + p$		central Au + Au	
	π^0	γ_{rich}	π^0	γ_{rich}
[9,11]	12869	15232	40437	83804
[11,15]	4918	7328	14262	42279
[15,20]	699	1522	1553	8353

The semi-inclusive recoil-jet distribution corresponding to pure γ_{dir} triggers is then determined statistically from the π^0 - and γ_{rich} -triggered recoil-jet distributions (Sect. 8).

6 Jet reconstruction

Jet reconstruction utilizes the approach described in Ref. [49], for both $p + p$ and central Au + Au collisions. As discussed in Sect. 4.2, in central Au + Au collisions the correction for uncorrelated background yield is carried out statistically, i.e. at the level of ensemble-averaged distributions, without discrimination of individual jets as signal or background. The output of the jet reconstruction algorithm is therefore referred to as a population of “jet candidates.”

The analysis is carried out in several steps, each with a different specification of $p_{T,\text{jet}}$. To distinguish the different types of jet candidate we utilize the notation defined in Ref. [49]: $p_{T,\text{jet}}^{\text{raw}}$ refers to $p_{T,\text{jet}}$ generated by the jet reconstruction algorithm; $p_{T,\text{jet}}^{\text{reco,ch}}$ is $p_{T,\text{jet}}^{\text{raw}}$ adjusted by ρA_{jet} (Eq. 6), the estimated uncorrelated background contribution; and $p_{T,\text{jet}}^{\text{ch}}$ is p_T of jet candidates after full correction for the effects of instrumental response and background fluctuations. For the simulation of $p + p$ collisions, $p_{T,\text{jet}}^{\text{part,ch}}$ is the reconstructed jet energy at the particle-level and $p_{T,\text{jet}}^{\text{det,ch}}$ is at the detector level.

Jets are reconstructed from accepted charged tracks using the k_T [8] and anti- k_T [61] algorithms with the E -recombination scheme [8]. Jet area is measured using the FastJet active-area approach with ghost-particle area of 0.01 [93].

In both $p + p$ and central Au + Au collisions, jet reconstruction is carried out twice. The first reconstruction pass uses the k_T algorithm with $R = 0.2$ and 0.5 to estimate the background transverse-momentum density in the event [88],

$$\rho = \text{median} \left\{ \frac{p_{T,\text{jet}}^{\text{raw},i}}{A_{\text{jet}}^i} \right\}, \quad (5)$$

where i labels the jets in the event, and $p_{T,\text{jet}}^{\text{raw},i}$ and A_{jet}^i are the transverse momentum and area of jet i . The median is calculated by excluding the hardest jet in the event for $p + p$ collisions, and the two hardest jets for central Au + Au collisions [49].

The second jet reconstruction pass is then carried out using the anti- k_T algorithm with $R = 0.2$ and 0.5 . Jet candidates from the second pass are accepted for further analysis if their centroid satisfies $|\eta| < 1 - R$. The value of $p_{T,\text{jet}}^{\text{raw}}$ from this pass is adjusted for the estimated background transverse-momentum density according to

$$p_{T,\text{jet}}^{\text{reco},i} = p_{T,\text{jet}}^{\text{raw},i} - \rho \times A_{\text{jet}}^i. \quad (6)$$

In $p + p$ collisions, for $R = 0.2$ the most probable value of ρ is zero, while for $R = 0.5$ the term $\rho \times A_{\text{jet}}^i$ is rarely greater than 1 GeV/ c . For central Au + Au collisions the value of ρ varies between 15 and 40 GeV/ c (Fig. 3), largely independent of the choice of R for calculating ρ .

6.1 Event mixing

Correction for the uncorrelated jet yield in central Au + Au collisions is carried out by subtracting the normalized ME $p_{T,\text{jet}}^{\text{reco, ch}}$ distribution from that of the same-event (SE) population, following the procedure described in [49]. In brief, event mixing creates synthetic events made up of tracks from real events, but with no two tracks in each mixed event originating from the same real event. The ME population therefore reproduces the detailed features of real events at the ensemble-averaged level but does not contain any multi-hadron correlations, including jets. The analysis is then carried out on the ME population, with the resulting distributions of “jets” providing the measurement of the contribution of purely combinatorial jet candidates to the jet candidate population in the analysis of real data.

In this analysis, event mixing utilizes 5 bins in multiplicity, 18 bins in z_{vtx} , 2 bins in event-plane orientation, and three bins in run-averaged luminosity, for a total of 540 distinct mixing classes. As in Ref. [49], no jet candidates are excluded from the ρ calculation for ME events.

6.2 ρ alignment

At low $p_{\text{T,jet}}^{\text{reco,ch}}$ the uncorrelated background is a large fraction of the total yield, and the ME subtraction therefore corresponds to taking a small difference of two large numbers. Since the recoil-jet distribution varies rapidly as a function of $p_{\text{T,jet}}^{\text{reco,ch}}$, it is therefore crucial that the $p_{\text{T,jet}}^{\text{reco,ch}}$ scales of the SE and ME distribution are well-aligned [49].

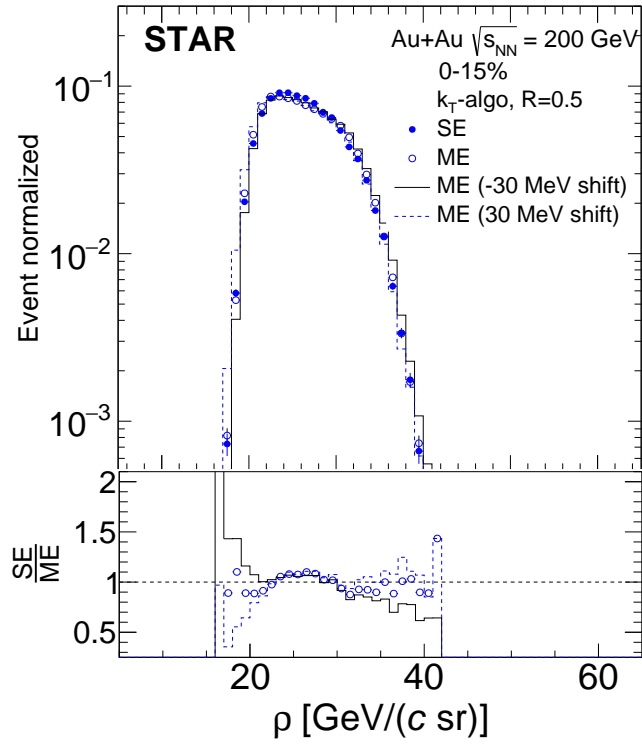


Figure 3: Upper panel: distribution of ρ ($R = 0.5$) in γ_{rich} -triggered central Au + Au collisions for the SE and ME populations, for ρ -shift values 0 and ± 30 MeV (Sect. 7). Lower panel: ratio of the SE and ME distributions.

The definition of ρ (Eq. 5) contains arbitrary choices, and ρ is not absolutely defined. In addition, the ρ distributions for SE and ME may differ, since the hard jet components of the SE and ME events populations differ. As shown in Ref. [49], precise alignment of the $p_{T,\text{jet}}^{\text{reco,ch}}$ scale for the SE and ME populations can be achieved in a data-driven way, by shifting the ME ρ distribution horizontally by a small amount. Figure 3 shows the distribution of ρ for SE and ME events in γ_{rich} -triggered central Au + Au collisions, for ρ -shift values of zero and ± 30 MeV. The figure shows that, in practice, a ρ -shift value of zero is close to optimal for this event selection, with a precision of ~ 30 MeV.

6.3 Jet area

Figure 4 shows the distribution of $p_{T,\text{jet}}^{\text{reco,ch}}$ vs. jet area for SE and ME events in central Au + Au collisions, and for $p + p$ collisions. Figure 5 shows the projection of the distributions in Fig. 4 onto the A_{jet} axis for the γ_{rich} -triggered populations with $R = 0.5$. The SE and ME distributions for central Au + Au collisions agree in detail, consistent with [49]. Both distributions, as well as those for $p + p$ collisions, are peaked close to the value $\pi R^2 = 0.785$. Small-area clusters predominantly have $p_{T,\text{jet}}^{\text{reco,ch}} \sim 0$, as shown in Fig. 4, and largely do not correspond to physical jets [49]. This background is suppressed by imposing a cut $A_{\text{jet}} > 0.05$ for $R = 0.2$ and $A_{\text{jet}} > 0.65$ for $R = 0.5$, with the latter shown in Fig. 5.

7 Raw distributions and Mixed Events

Figure 6 shows uncorrected semi-inclusive recoil-jet distributions for $R = 0.2$ and 0.5 as a function of $p_{T,\text{jet}}^{\text{reco,ch}}$, for γ_{rich} -triggered and π^0 -triggered $p + p$ collisions at $\sqrt{s} = 200$ GeV in the defined $E_{\text{T}}^{\text{trig}}$ bins. Larger $E_{\text{T}}^{\text{trig}}$ corresponds to a harder recoil-jet spectrum, as expected. For π^0 triggers with $E_{\text{T}}^{\text{trig}} = 15$ -20 GeV, the recoil-jet spectra are not shown because, due to limited trigger statistics (Tab. 1) the unfolding does not converge, and results for this $E_{\text{T}}^{\text{trig}}$ bin are not presented in Sect. 13.1.

Uncorrected semi-inclusive recoil-jet distributions for central Au + Au collisions are shown in Fig. 7 for γ_{rich} triggers and in Fig. 8 for π^0 triggers. In all cases the recoil-jet yield at large positive $p_{T,\text{jet}}^{\text{reco,ch}}$ is larger for higher $E_{\text{T}}^{\text{trig}}$ values, as expected for correlated jet yields, while at lower $p_{T,\text{jet}}^{\text{reco,ch}}$ the

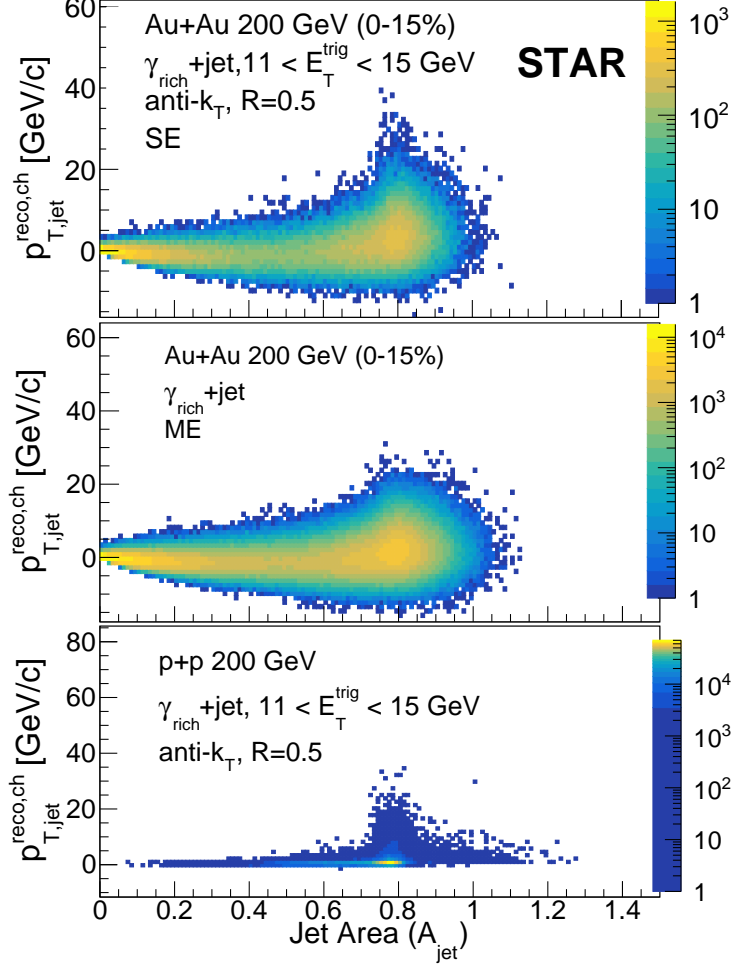


Figure 4: Distribution of $p_{T,jet}^{\text{reco,ch}}$ vs. jet area for γ_{rich} -triggered recoil jets, $R = 0.5$. Top: SE for central Au + Au collisions; middle: ME for central Au + Au collisions; bottom: $p + p$ collisions.

distributions are very similar for the different E_T^{trig} intervals. These features were also observed in Ref. [40, 49].

Figures 7 and 8 also show $p_{T,jet}^{\text{reco,ch}}$ distributions for ME populations, with the hatched region showing the ME normalization range. Figures 7 and 8, bottom panels, show that the yield ratio SE/ME in the far negative $p_{T,jet}^{\text{reco,ch}}$

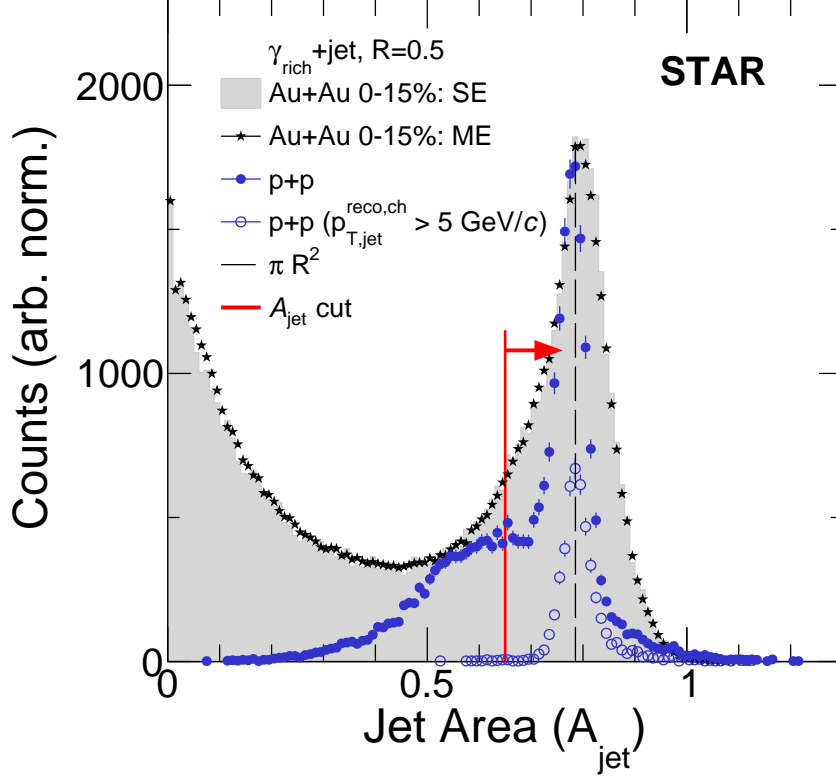


Figure 5: Projection of distributions in Fig. 4 onto the A_{jet} axis, for γ_{rich} -triggered recoil jets with $R = 0.5$ for SE and ME in Au + Au collisions and for $p + p$ collisions. The vertical red line shows the A_{jet} acceptance cut, $A_{\text{jet}} > 0.65$. The dashed black line indicates πR^2 for $R = 0.5$.

region has weak (for $R = 0.2$) or negligible (for $R = 0.5$) dependence on $p_{\text{T,jet}}^{\text{reco,ch}}$, as expected if this region is dominated by uncorrelated background yield [40, 49]. This region is therefore used to normalize the ME distribution. The ensemble-averaged distribution of trigger-correlated recoil-jet yield is given by the difference of the SE and normalized ME distributions [40, 49].

Table 2 gives the recoil-jet yield integrals of the SE and ME distributions prior to normalization, which agree within $\sim 1\%$. Such invariance of the recoil-jet yield integral (or equivalently, jet density) has been observed in other high-multiplicity analyses [40, 49]. This invariance is consistent with the resilience of anti- k_{T} jet reconstruction against distortion by large back-

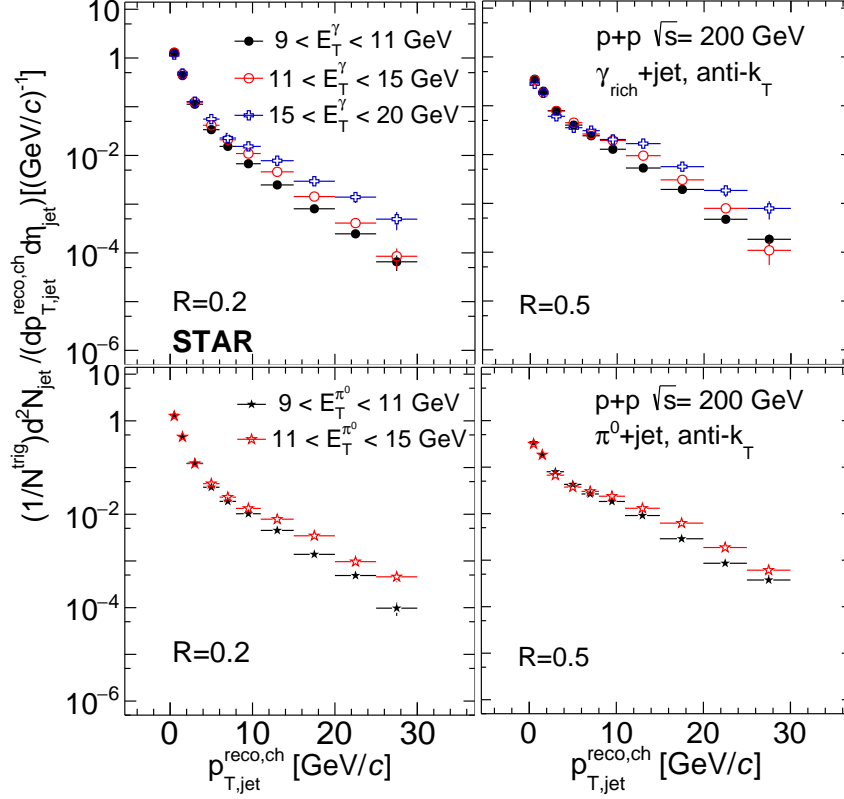


Figure 6: (Color online) Uncorrected semi-inclusive recoil-jet distributions for selected E_T^{trig} intervals and recoil jet $R = 0.2$ (left) and 0.5 (right), for γ_{rich} -triggered (top) and π^0 -triggered (bottom) $p + p$ collisions at $\sqrt{s} = 200$ GeV.

grounds [61], and it plays an important role in this analysis approach. Table 2 also gives the values of the ME normalization factor f^{ME} , which are similar to those in Ref. [49].

Figure 9 shows the result of subtracting the normalized ME distributions from the SE distributions in Figs. 7 and 8. These are distributions after correction for uncorrelated background yield, and used in the further analysis. Because the vertical axes have logarithmic scale, bins with negative values from the subtraction cannot be shown; however, these bins all have values consistent with statistical fluctuations.

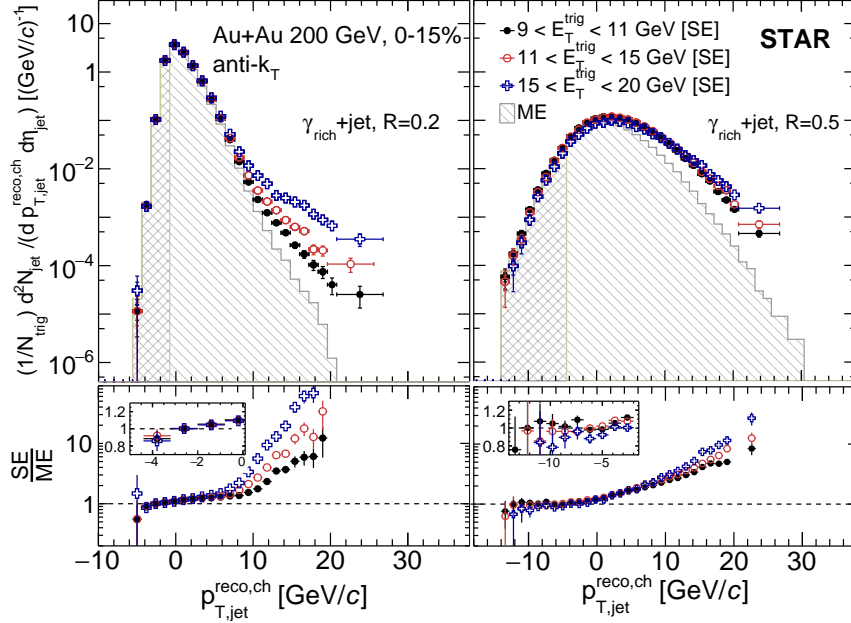


Figure 7: (Color online) Upper panels: uncorrected semi-inclusive recoil-jet distributions for γ_{rich} -triggered central Au + Au collisions at $\sqrt{s_{\text{NN}}} = 200$ GeV in the $E_{\text{T}}^{\text{trig}}$ bins of the analysis, for $R = 0.2$ (left) and 0.5 (right). Colored markers show data (SE); histograms show normalized Mixed Event (ME) distributions. The hatched distribution is the ME normalization region. Lower panels: ratio of SE/ME. Insets show the ratio of SE/ME in the ME normalization region with linear vertical scale.

Since the subtraction at low and negative values of $p_{\text{T,jet}}^{\text{reco, ch}}$ corresponds to taking a small difference of two large numbers, large oscillations can arise if the two distributions are not aligned precisely. However, all difference distributions in Fig. 9 are seen to be well-behaved, without large oscillations or other non-monotonic features at low $p_{\text{T,jet}}^{\text{reco, ch}}$, which provides independent validation of the ρ alignment discussed in Sect. 6.2.

8 Extraction of $\gamma_{\text{dir}} + \text{jet}$ distributions

The γ_{rich} -trigger population is an admixture of direct photons, decay photons from asymmetrically decaying π^0 and from η decays, and fragmentation

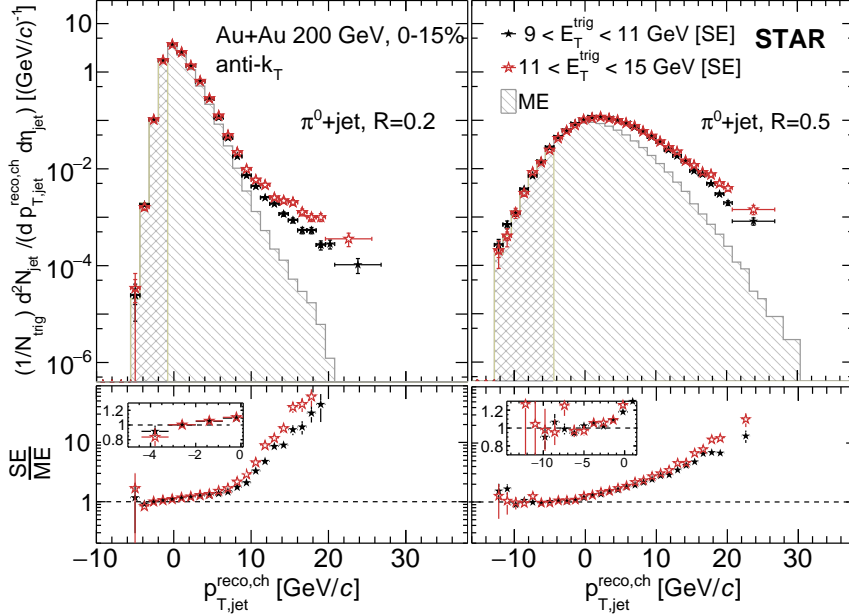


Figure 8: (Color online) The same as Fig. 7, for π^0 -triggered central Au + Au collisions.

photons. As mentioned in Sect. 5, the ansatz that direct photons have no near-side correlated hadron yield is used to correct $\gamma_{\text{rich}}+\text{jet}$ to $\gamma_{\text{dir}}+\text{jet}$ distributions, with the $\pi^0+\text{jet}$ yield used as a measure of the jets recoiling from background triggers. This is the same method as was used in Ref. [58].

The γ_{dir} -triggered semi-inclusive recoil-jet yield, $\mathcal{D}_{\gamma_{\text{dir}}}(p_{\text{T}})$, is defined as

$$\mathcal{D}_{\gamma_{\text{dir}}}(p_{\text{T},\text{jet}}) = \frac{\mathcal{D}_{\gamma_{\text{rich}}}(p_{\text{T},\text{jet}}) - R_{\text{impurity}} \cdot \mathcal{D}_{\pi^0}(p_{\text{T},\text{jet}})}{1 - R_{\text{impurity}}}. \quad (7)$$

Here $\mathcal{D}_{\gamma_{\text{dir}}}(p_{\text{T},\text{jet}})$, $\mathcal{D}_{\gamma_{\text{rich}}}(p_{\text{T},\text{jet}})$, and $\mathcal{D}_{\pi^0}(p_{\text{T},\text{jet}})$ represent the trigger-normalized recoil-jet yield as a function of $p_{\text{T},\text{jet}}$ for γ_{dir} , γ_{rich} , and π^0 triggers, respectively. The factor $(1-R_{\text{impurity}})$ represents the purity of γ_{dir} in the γ_{rich} sample. The purity of the π^0 -trigger sample is estimated from simulation to be greater than $\sim 95\%$ for all $E_{\text{T}}^{\text{trig}}$ bins, satisfying the high-purity condition necessary for this correction procedure. Systematic studies show negligible dependence of the fully corrected recoil-jet spectrum on the value of π^0 purity between 95 and 100%.

The calculation of $\mathcal{D}_{\gamma_{\text{dir}}}(p_{\text{T},\text{jet}})$ can be performed both on the corrected

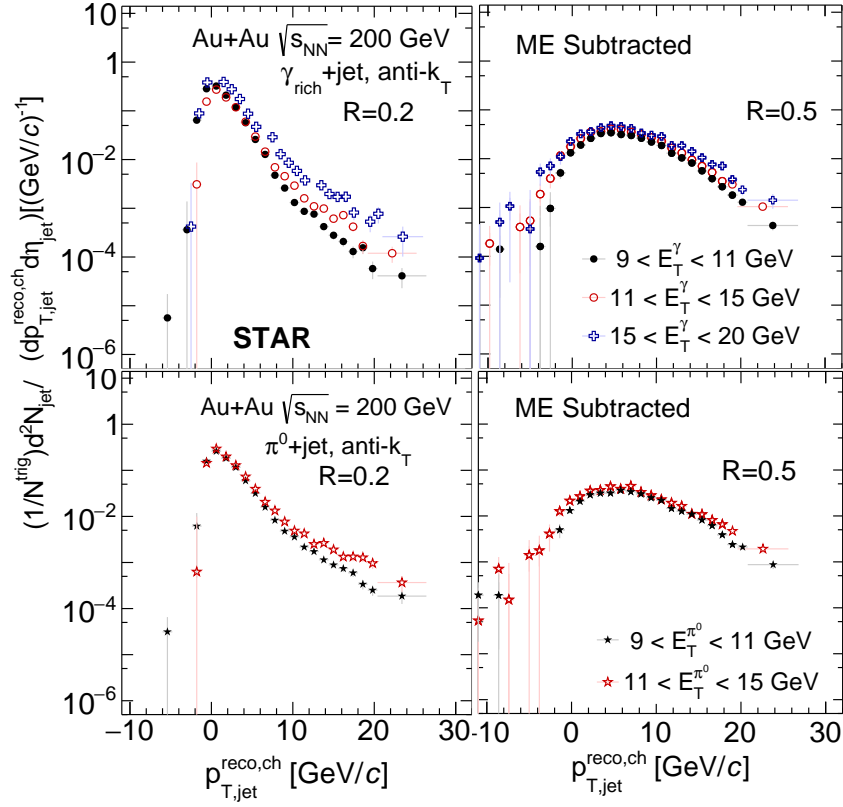


Figure 9: (Color online) Recoil-jet distributions for central Au+Au collisions after subtraction of normalized ME distributions. Data are from Fig. 7 and 8. Upper: γ_{rich} triggers; lower: π^0 triggers. Left: $R = 0.2$; right: $R = 0.5$. Negative values after subtraction not shown, due to logarithmic vertical axis.

Table 2: Integral of SE and ME distributions, ME normalization region, and ME normalization factor f^{ME} for all $E_{\text{T}}^{\text{trig}}$ bins for the γ_{rich} and π^0 triggers, and for recoil jet $R = 0.2$ and 0.5 .

Trigger	R	$E_{\text{T}}^{\text{trig}}[\text{GeV}]$	Integral		ME norm [GeV/ c]	f^{ME}
			SE	ME		
γ_{rich}	0.2	[9,11]	12.72	12.60	[-10,2]	0.80 ± 0.03
		[11,15]	12.73	12.60	[-10,2]	0.83 ± 0.04
		[15,20]	12.73	12.60	[-10,2]	0.79 ± 0.03
	0.5	[9,11]	1.22	1.18	[-20,-5]	0.72 ± 0.01
		[11,15]	1.23	1.19	[-20,-5]	0.74 ± 0.02
		[15,20]	1.23	1.18	[-20,-5]	0.70 ± 0.02
π^0	0.2	[9,11]	12.73	12.64	[-10,2]	0.83 ± 0.01
		[11,15]	12.72	12.64	[-10,2]	0.84 ± 0.02
	0.5	[9,11]	1.23	1.17	[-20,-5]	0.73 ± 0.02
		[11,15]	1.23	1.17	[-20,-5]	0.70 ± 0.03

(unfolded) recoil-jet spectra, and on the raw spectra before unfolding. If statistics are limited, subtraction before unfolding is preferable because unfolding may not converge. For Au + Au collisions, the default method is to subtract the unfolded π^0 -triggered spectrum from the unfolded γ_{rich} +jet spectrum, for all $E_{\text{T}}^{\text{trig}}$ bins except $E_{\text{T}}^{\text{trig}}=15\text{-}20$ GeV. For $E_{\text{T}}^{\text{trig}}=15\text{-}20$ GeV, the π^0 -triggered recoil-jet spectrum is not statistically precise enough for unfolding to converge reliably, so subtraction is carried out before unfolding. For $p + p$ collision, the default method for all $E_{\text{T}}^{\text{trig}}$ bins is to subtract before unfolding. Where possible, the alternate method was checked for consistency with the default method.

The purity of γ_{dir} triggers in the γ_{rich} population is determined by applying the ansatz that γ_{dir} triggers do not have a correlated near-side yield of charged hadrons within relative azimuthal angle $\Delta\varphi < 1.4$. The fraction of background triggers is then determined statistically for each $E_{\text{T}}^{\text{trig}}$ bin using the near-side correlated charged-hadron yields, as was done in Ref. [58].

The ratio of correlated yields is defined as

$$R_{\text{impurity}} = \frac{Y_{\gamma_{\text{rich}}+h}^{\text{near}}}{Y_{\pi^0+h}^{\text{near}}}, \quad (8)$$

where $Y_{\gamma_{\text{rich}}+h}^{\text{near}}$ is the near-side ($\Delta\varphi \leq 1.4$ rad) yield of charged hadrons per

γ_{rich} trigger and $Y_{\pi^0+h}^{\text{near}}$ is the near-side yield per π^0 trigger, after subtracting the uncorrelated background of charged hadrons. The value of R_{impurity} is determined for different ranges of $z_{\text{T}} = p_{\text{T,track}}/E_{\text{T}}^{\text{trig}}$, for $z_{\text{T}} > 0.1$ and $p_{\text{T,track}} > 1.2 \text{ GeV}/c$. The uncorrelated background is determined from the measured yield outside of the near-side peak region in $\Delta\varphi$, where this region is varied to determine the systematic uncertainty in the uncorrelated background subtraction. At low z_{T} , where the relative uncorrelated yield is high, this is the dominant uncertainty, while at high z_{T} the statistical error dominates. For each $E_{\text{T}}^{\text{trig}}$ selection, the value of R_{impurity} is determined from averaging the ratios (Eq. 8) for the different z_{T} ranges. The uncertainty in R_{impurity} includes the uncertainty in the uncorrelated background subtraction.

All correlated charged tracks for γ_{rich} triggers are attributed to background (π^0 , photons from π^0 and η decays, and fragmentation photons) in the trigger sample. The subtraction of the recoil-jet yield due to background triggers (Eq. 7) is carried out assuming that the correlated yield and the recoil-jet distribution associated with the background triggers is the same as that measured for π^0 triggers.

We assume that the recoil-jet distribution for high- p_{T} η -meson triggers is the same as that for π^0 -meson triggers, based on both simulation and η measurements at RHIC [94,95]. This assumption also applies to photons from π^0 and η decays because the trigger requirement biases towards asymmetric decay, such that the decay photon carries most of the parent-meson energy. This was verified in simulation by comparing the mean E_{T} of the parent meson, for which the decay photon falls within a given $E_{\text{T}}^{\text{trig}}$ selection, to the mean E_{T} of the symmetrically decaying π^0 that passes the TSP cut and falls into the same $E_{\text{T}}^{\text{trig}}$ selection. For $9 < E_{\text{T}}^{\text{trig}} < 11$ and $11 < E_{\text{T}}^{\text{trig}} < 15 \text{ GeV}$, the difference is approximately 5%, while it is $\sim 3\%$ for $15 < E_{\text{T}}^{\text{trig}} < 20 \text{ GeV}$. However, the associated-hadron yield for fragmentation photons is not well known. Therefore, the fragmentation photons are only subtracted to the extent that their near-side correlated hadron yields are similar to those of π^0 .

For central Au + Au collisions, the purity of γ_{dir} in the γ_{rich} sample varies between $67 \pm 3\%$ and $84 \pm 4\%$, from lowest to highest $E_{\text{T}}^{\text{trig}}$. For $p + p$ collisions, the purity of γ_{dir} varies between $43 \pm 5\%$ and $53 \pm 7\%$, from lowest to highest $E_{\text{T}}^{\text{trig}}$. The higher value of γ_{dir} purity in the central Au + Au data compared to $p + p$ data arises from the suppression of π^0 yield due to jet quenching in Au + Au collisions [96].

9 E_T^{trig} resolution

The γ_{dir} and π^0 -trigger particles are measured using the BEMC and BSMD detectors (Sect. 5). The measurement of E_T^{trig} is affected by the intrinsic energy resolution of the BEMC and by energy leakage to neighboring towers that is not accounted for by the clustering algorithm. To quantify this distortion, the Trigger Energy Scale (TES) and Trigger Energy Resolution (TER) are determined using the STAR GEANT3 simulation.

This study utilizes a simple particle gun simulation, in which single π^0 and γ particles are generated with a uniform E_T distribution in the range $6 < E_T < 30$ GeV, and with uniform spatial distribution on a regular grid in (η, ϕ) , with spacing of 0.6 radians (12 towers) and 0.3 radians (6 towers) for π^0 and γ particles, respectively. This approach enables multiple particles to be simulated per event without overlapping signals in the BEMC. The larger spacing for π^0 prevents overlap of decay photons from other π^0 . The generated events are then passed through the STAR GEANT3 simulation with the detector configuration corresponding to the 2009 $p + p$ run.

The simulated BEMC showers for γ and π^0 particles are clustered with the same algorithm as is used for data, applying the same TSP cuts. Clusters are matched to the simulated particles in (η, ϕ) phase space, based on the projected position of the particle on the face of the BEMC towers.

We denote E_T of the γ and π^0 at the generated level as $E_T^{\gamma, \text{part}}$ and $E_T^{\pi^0, \text{part}}$; at the reconstructed level as $E_T^{\gamma, \text{det-clust}}$ and $E_T^{\pi^0, \text{det-clust}}$; and at the matched level as $E_T^{\gamma, \text{part-match}}$ and $E_T^{\pi^0, \text{part-match}}$. Note that the matched-level E_T is the generated-level E_T for a particle reconstructed within our selection ranges.

The values of the TES and TER are determined from the ratio of the reconstructed to the generated E_T for matched clusters,

$$q_T = \frac{E_T^{\gamma, \text{det-clust}}}{E_T^{\gamma, \text{part-match}}}, \quad (9)$$

similarly for π^0 . The q_T distribution is calculated by weighting the uniformly-generated particles by a physical E_T distribution. The resulting q_T distribution is fit with a Gaussian function, the mean of which is the TES and the RMS of which is the TER.

Table 3 gives the values of TES and TER for π^0 and γ in the E_T^{trig} bins of this analysis. The TES values for π^0 are smaller than those for γ , due to larger probability of energy leakage into neighboring towers that is not

Table 3: TES and TER of triggers in the bins of $E_T^{\text{det-clust}}$, from fitting the q_T distributions (Eq. 9). The uncertainty shown is statistical only. The relative systematic uncertainty is approximately 3% for TES and 5% for TER. The average E_T for each selection is calculated using the smearing weights, assuming the trigger spectrum shape given by PYTHIA-6 STAR tune.

$E_T^{\text{det-clust}}$ [GeV]	π^0			γ		
	TES (%)	TER (%)	$\langle E_T \rangle$ [GeV]	TES (%)	TER (%)	$\langle E_T \rangle$ [GeV]
9 - 11	92.4 ± 0.2	9.1 ± 0.1	10.5	97.97 ± 0.05	8.12 ± 0.03	10.2
11 - 15	94.4 ± 0.2	8.4 ± 0.1	11.8	97.77 ± 0.03	7.83 ± 0.02	12.7
15 - 20				97.74 ± 0.03	7.56 ± 0.02	16.8

recovered by the clustering algorithm. Table 3 also gives values of $\langle E_T \rangle$ for different trigger selections, calculated using the smearing weights, assuming the trigger spectrum shape for E_T^{part} is that generated by PYTHIA-6 STAR tune. For π^0 triggers with $9 < E_T^{\text{trig}} < 11$ GeV, the mean $E_T^{\text{part-match}}$ is higher than the mean E_T of the physical spectrum (9.8 GeV) in the interval $9 < E_T < 11$ GeV. However, for π^0 with $11 < E_T^{\text{trig}} < 15$ GeV, the mean $E_T^{\text{part-match}}$ is lower than the mean E_T of the physical spectrum (12.2 GeV) due to the TSP selection bias toward wider π^0 showers. The TSP selection biases the π^0 population to lower E_T^{trig} , which has larger opening angle on average.

The trigger resolution arises from the intrinsic responses of the BEMC and BSMD, which at high E_T experience negligible influence from the overall event environment. The values of TES and TER should therefore be similar for $p + p$ and central Au + Au collisions. This was studied by comparing q_T distributions for π^0 and γ found in PYTHIA-6 STAR tune di-jet events, embedded in the 2009 $p + p$ and the 2014 Au + Au data and analysed using the algorithm described in Sect. 5. For γ triggers the event background does not significantly shift or broaden the q_T distribution. For π^0 triggers, there is a small (1–3%) broadening of the resolution in the Au + Au events compared to $p + p$ events, but no significant shift in the scale.

No correction for TES and TER is applied in the data analysis. For precise comparison of theoretical calculations to the measurements, the calculated distributions should therefore be smeared to account for the TES and TER

effects. Weight factors are provided here for that purpose, to be applied bin-wise in E_T^{trig} to a theoretically calculated recoil-jet distribution. In order to be able to apply the weighting, the theory calculation should record recoil jets for triggers with E_T between 6 and 30 GeV, storing the recoil-jet spectrum in 1 GeV increments of E_T^{trig} . The weights W are defined as the relative probability of a photon with calculated value E_T^{part} to contribute to a bin in measured $E_T^{\text{det-clust}}$,

$$\begin{aligned} W(E_T^{\text{part}}; E_T^{\text{det-clust}}) &= P(E_T^{\text{det-clust}} | E_T^{\text{part}}) \\ &= P(E_T^{\text{part}} | E_T^{\text{det-clust}}) \frac{P(E_T^{\text{det-clust}})}{P(E_T^{\text{part}})}, \end{aligned} \quad (10)$$

where the last expression uses Bayes's Theorem.

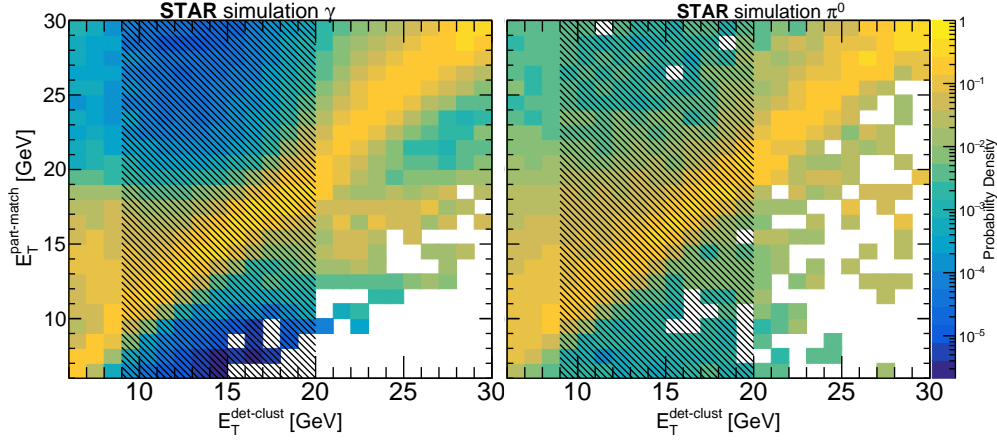


Figure 10: Distribution of E_T^{trig} at the matched (vertical) vs. reconstructed (horizontal) levels for γ_{dir} (left) and π^0 triggers (right). The hashed boxes indicate the E_T^{trig} selection used in this analysis.

Figure 10 shows the 2-D correlation of matched (generated) E_T vs. reconstructed (detector-level) E_T , with a uniform (flat) distribution in E_T^{part} . Vertical slices in this distribution represent the probability distribution for a bin of generated-level E_T ($E_T^{\text{part-match}}$) to contribute to the bin of detector-level E_T ($E_T^{\text{det-clust}}$). The weight factors $W(E_T^{\text{part}}; E_T^{\text{det-clust}})$ are calculated from the 2-D distribution in using the last expression in Eq. 10, by projecting out the $E_T^{\text{part-match}}$ distributions for a given selection of $E_T^{\text{det-clust}}$ (e.g.

11–15 GeV). This selection interval in $E_T^{\text{det-clust}}$ corresponds to the factor $P(E_T^{\text{det-clust}})$ in Eq. 10.

Since a uniform E_T^{part} distribution is used to generate Fig. 10, the factor $P(E_T^{\text{part}})$ is simply a scaling factor that has no effect on the relative weighting. The integral of $W(E_T^{\text{part}}; E_T^{\text{det-clust}})$ for each selection in $E_T^{\text{det-clust}}$ is therefore arbitrarily normalized to unit integral. This distribution is the relative weight factor to be applied as a function of E_T^{part} for a given selection in $E_T^{\text{det-clust}}$. The distributions for both trigger types and all E_T^{trig} ranges are shown in Fig. 11.

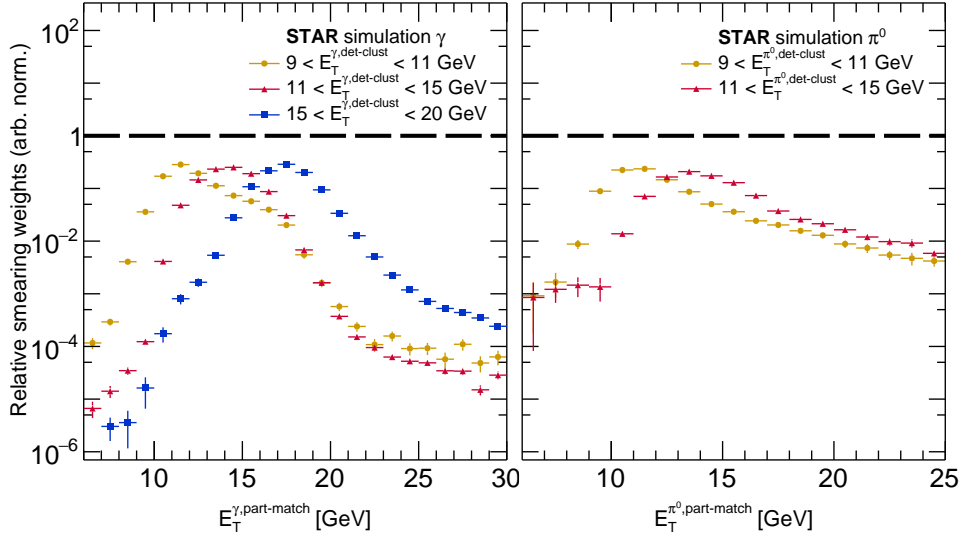


Figure 11: E_T^{trig} smearing weights for γ_{dir} (left panel) and π^0 triggers (right panel).

As an example, Fig. 12 shows the effect of scaling a physical trigger- E_T^{part} spectrum generated by PYTHIA by $W(E_T^{\text{part}}; E_T^{\text{det-clust}})$ from Fig. 11. The generated trigger spectra for photons (left) and π^0 (right) are shown as black stars. The other markers show the resulting distributions of $E_T^{\text{part-match}}$ for the different bins of E_T^{trig} , with the weight factors from Fig. 11 applied to the E_T^{part} . These distributions have been normalized to conserve the number of triggers. For example, for the detector-level selection $11 < E_T^{\text{det-clust}} < 15$ GeV, the integral over $6 < E_T^{\text{part-match}} < 30$ GeV is equal to the integral over $11 < E_T^{\text{part}} < 15$ GeV.

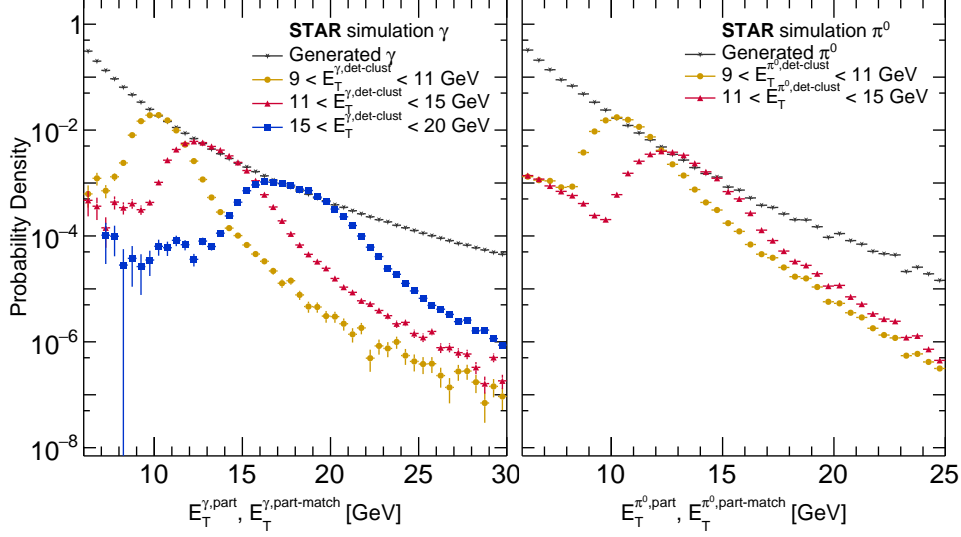


Figure 12: Generated vs. smeared E_T^{trig} distributions for γ_{dir} (left panel) and π^0 triggers (right panel).

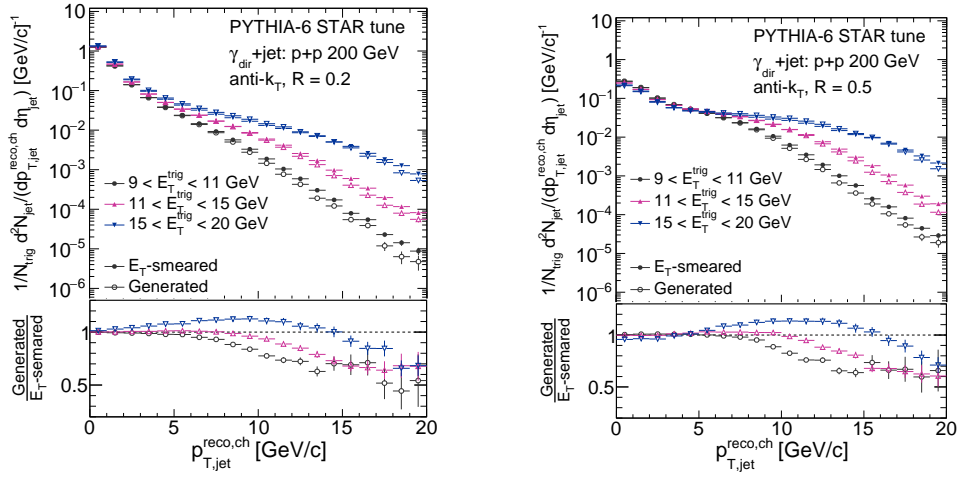


Figure 13: Effect of TES/TER on γ_{dir} -triggered recoil jets in $p + p$ collisions at $\sqrt{s} = 200$ GeV with $R = 0.2$ (left) and 0.5 (right), simulated using PYTHIA-6 STAR tune. Open markers denote the jet spectra without E_T weights, and filled markers denote the jet spectra after E_T reweighting.

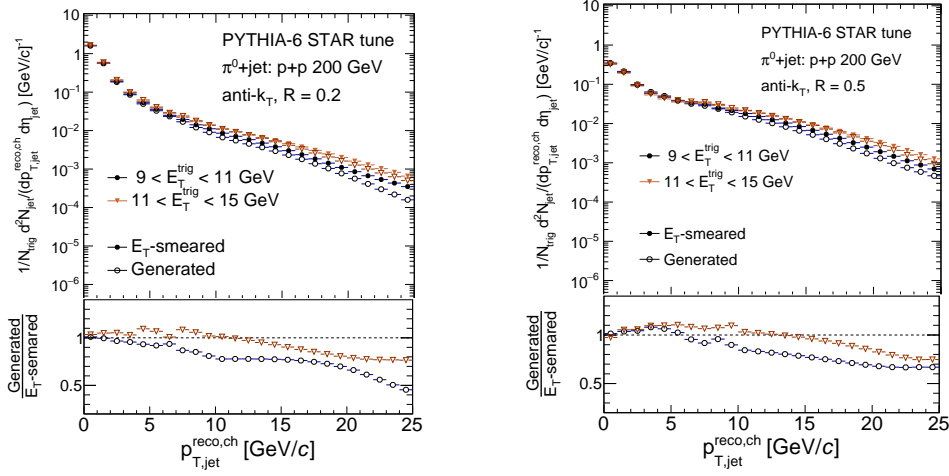


Figure 14: Same as Fig. 13, for π^0 triggers.

To illustrate the effect of the TES/TER on the recoil-jet spectra, the weighting factors in Fig. 11 are applied to E_T^{trig} -dependent jet spectra from PYTHIA-6 STAR tune. Figures 13 and 14 show PYTHIA-6 STAR tune recoil-jet spectra before (open markers) and after the E_T weighting (filled markers). For the open markers, γ_{dir} and π^0 triggers were selected in the E_T^{trig} ranges of this analysis. For the filled markers, γ_{dir} and π^0 were accepted for $6 < E_T^{\text{trig}} < 30$ GeV and then re-weighted for each E_T^{trig} selection, as described above. Note that simply restricting the E_T^{trig} range in order to match the sampled average E_T ($\langle E_T \rangle$ in Tab. 3) is not equivalent.

10 Corrections

The distribution of trigger-correlated jet yield is obtained by subtracting the normalized ME distribution from the SE distribution, as discussed in Sect. 7. This correlated-yield distribution must then be corrected for $p_{T,\text{jet}}$ -smearing due to instrumental effects in both $p + p$ and central Au + Au collisions, and to background fluctuations in central Au + Au collisions.

10.1 Instrumental effects

10.1.1 $p + p$ collisions

Instrumental effects for $p + p$ collisions at $\sqrt{s} = 200$ GeV are determined using simulated di-jet events generated by PYTHIA 6.42, Perugia 0 tune. These events are passed through the STAR GEANT3 simulation to produce detector-level events, which are embedded into real zero-bias $p + p$ collision events at $\sqrt{s} = 200$ GeV from the 2009 RHIC run to emulate pile-up effects.

Jet reconstruction is then carried out on both the particle-level and detector-level events. Recoil jets at the particle and detector levels are matched by requiring that the distance between jet axes $\delta R = \sqrt{\delta\varphi^2 + \delta\eta^2} < R$, and $0.5 < (p_{T,\text{jet}}^{\text{det,ch}} / p_{T,\text{jet}}^{\text{part,ch}}) < 1.3$. The jet-matching efficiency is the fraction of particle-level jets that are matched to detector-level jets.

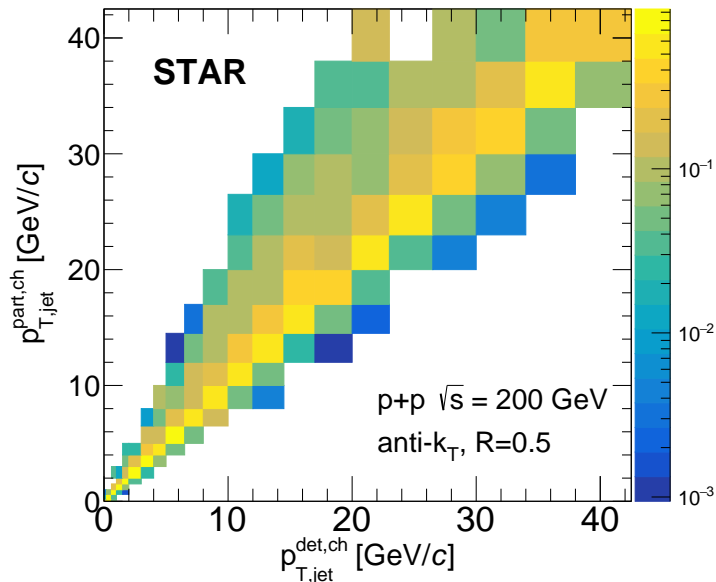


Figure 15: Response matrix, R_{instr} , for charged-particle jets with $R = 0.5$ in $p + p$ collisions at $\sqrt{s} = 200$ GeV.

Figure 15 shows R_{instr} , the response matrix for instrumental effects. The matrix is normalized such that the integral over $p_{T,\text{jet}}^{\text{det,ch}}$ is unity for each bin in $p_{T,\text{jet}}^{\text{part,ch}}$. Figure 16, upper panel, shows the jet-matching efficiency in $p + p$ collisions for $R = 0.2$ and 0.5 .

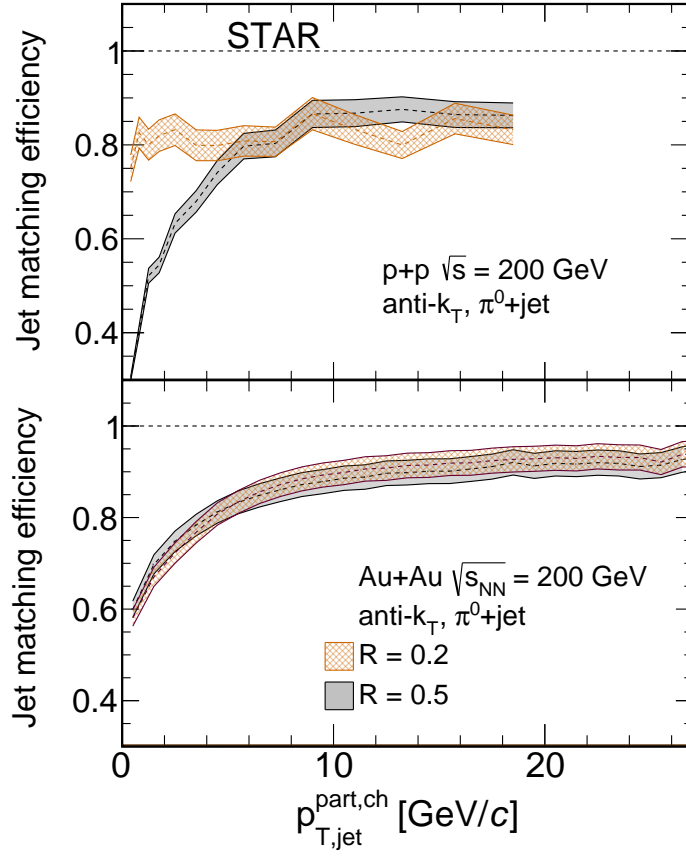


Figure 16: Jet matching efficiency as a function of $p_{T,jet}^{part,ch}$, in $p + p$ (upper) and central Au + Au (lower) collisions for recoil jets with $R = 0.2$ and 0.5 . The bands show the systematic uncertainties due to variation in the tracking efficiency. See text for discussion.

10.1.2 Au + Au collisions

The charged-particle tracking efficiency for central Au + Au collisions is determined by embedding detector-level simulated tracks for pions, kaons, and protons into real Au + Au events. The charged-particle tracking efficiency corresponds to the weighted average of efficiencies for individual species, with the weighting based on measurements of the relative inclusive particle yield for each species [97].

The instrumental response matrix R_{instr} is calculated using PYTHIA 8.185 to generate π^0 -triggered and γ_{dir} -triggered events for $p + p$ collisions at $\sqrt{s} = 200$ GeV. These particle-level events are passed through a fast simulator incorporating a parametrization of the charged-particle tracking response for Au + Au collisions. Jet reconstruction is run on the resulting detector-level particles. Matching between particle-level and detector-level recoil jets is carried out as described above for $p + p$ collisions, except that $p_{\text{T,jet}}^{\text{det,ch}}$ is only required to be at least 15% of $p_{\text{T,jet}}^{\text{part,ch}}$, consistent with [49]. Figure 16, lower panel, shows the jet-matching efficiency for central Au + Au collisions.

The jet-matching efficiencies for $p + p$ and Au+Au collisions in Fig. 16 differ significantly. These differences arise from the different criteria for matching particle- and detector-level jets, with more stringent matching requirement for $p + p$ collisions. In addition, the jet-matching efficiency for the small resolution-parameter jets ($R = 0.2$) in $p + p$ collisions approaches the single charged-particle efficiency and thus has a different shape than for $R = 0.5$. We note that the different matching criteria also generate differences in R_{instr} , with opposite effect, and it is only the combination of unfolding and the efficiency correction that is meaningful. Any residual dependence on the specific choice of matching criteria is accounted for in the systematic uncertainty.

Figure 17, upper panel, shows R_{instr} for recoil jets with $R = 0.5$ in central Au + Au collisions. The other panels are discussed below.

10.1.3 Jet energy scale and resolution

While the full instrumental response matrix, R_{instr} , is used to correct the measured recoil-jet spectrum via unfolding, it is nevertheless valuable to characterize the instrumental response qualitatively. The instrumental response is similar in this analysis to that reported in Ref. [49], for both $p + p$ and Au + Au collisions.

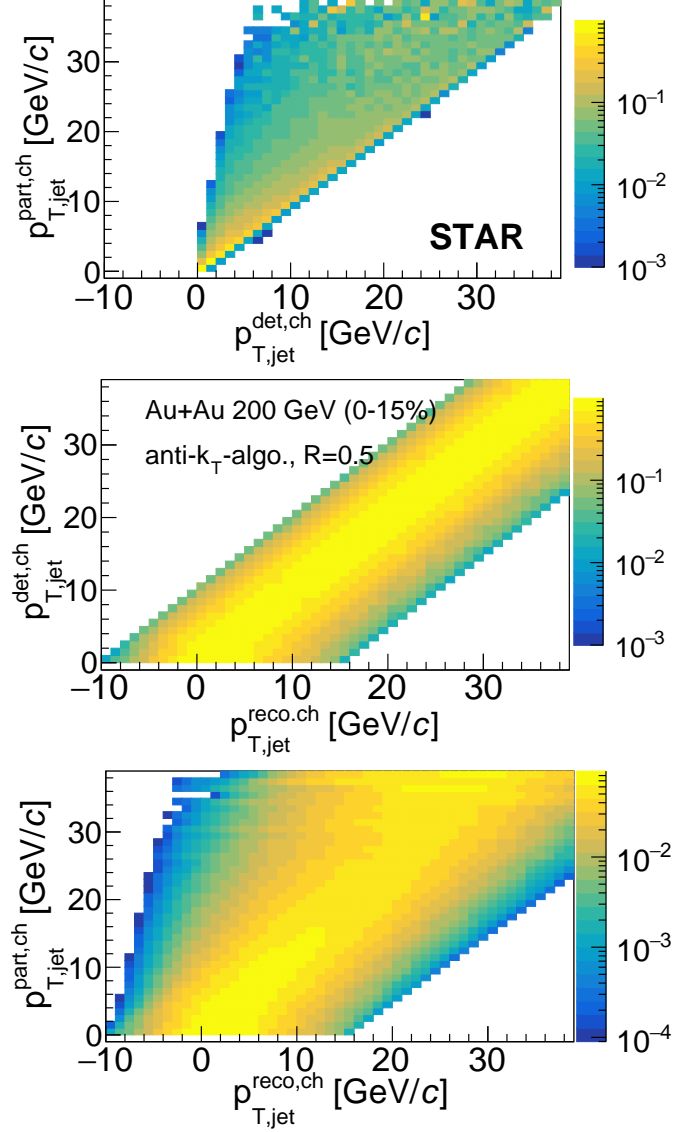


Figure 17: Response matrices for recoil jets with $R = 0.5$ in central Au + Au collisions with π^0 trigger. Top: instrumental response matrix R_{instr} ; middle: background fluctuation response matrix (SP embedding) R_{bkg} ; bottom: total response matrix R_{total} .

For charged-particle jets in the range $5 < p_{T,\text{jet}}^{\text{reco,ch}} < 30$ GeV/ c , the distribution characterizing jet energy resolution (JER) has RMS $\sim 25\%$, comprising a peak with width 5-10%, with an asymmetric tail to low jet energy, with negligible R -dependence. The jet energy scale (JES) uncertainty is 5%, likewise with negligible R -dependence.

10.2 Uncorrelated background: Au + Au collisions

We introduce the effect of uncorrelated background fluctuations on $p_{T,\text{jet}}^{\text{det,ch}}$, generating a distribution of $p_{T,\text{jet}}^{\text{reco,ch}}$ which models the measurement. This follows the embedding procedure outlined in [49], with three different classes of jet model used for systematic variation: PYTHIA-generated jets at the detector level; the same but with azimuthal correlation between trigger π^0 and the EP due to non-zero v_2 of the trigger hadron; and “Single Particle” (SP) jets in which one particle carries $p_{T,\text{jet}}^{\text{reco,ch}}$ and is collinear with the jet centroid.

As shown in Refs. [40, 49, 82], the background response matrices for inclusive and semi-inclusive jet observables calculated by embedding PYTHIA-generated jets and SP jets are very similar, demonstrating that jet reconstruction in the heavy-ion environment is largely independent of the specific fragmentation distribution of the jet population. This in turn indicates that corrections based on this embedding procedure are likewise valid for inclusive and semi-inclusive observables of quenched jets, whose fragmentation distribution is *a priori* unknown. We utilize SP embedding for the primary analysis, because it provides the clearest criteria for matching particle and detector-level jets.

The uncorrelated background is, per definition, the same for γ_{dir} -triggered and π^0 -triggered events, except for a possible EP bias. However, the EP bias in central Au + Au collisions has been shown to be negligible for charged-hadron triggers [49], with the same finding in this analysis. No significant difference is observed in the response matrices for γ_{dir} -triggered and π^0 -triggered events. We therefore focus on the response matrix for π^0 -triggered events, which is used to unfold both the γ_{dir} -triggered and π^0 -triggered distributions. Figure 17, middle panel, shows R_{bkg} for π^0 -triggered central Au + Au collisions using SP embedding, for $R = 0.5$.

10.3 Unfolding

10.3.1 Formalism

The $p_{T,\text{jet}}^{\text{reco,ch}}$ distribution is first corrected for uncorrelated yield by subtracting the normalized ME distribution (Sect. 7) giving the vector M , the measured distribution of correlated yield. M is related to the Truth distribution T according to

$$M(p_{T,\text{jet}}^{\text{reco,ch}}) = R_{\text{total}} \left(p_{T,\text{jet}}^{\text{reco,ch}}, p_{T,\text{jet}}^{\text{part,ch}} \right) \times T(p_{T,\text{jet}}^{\text{part,ch}}), \quad (11)$$

where R_{total} represents the cumulative response matrix from both the instrumental and heavy-ion background fluctuations. We assume that R_{total} factorizes [49], such that

$$R_{\text{total}} \left(p_{T,\text{jet}}^{\text{reco,ch}}, p_{T,\text{jet}}^{\text{part,ch}} \right) = R_{\text{bkg}} \left(p_{T,\text{jet}}^{\text{reco,ch}}, p_{T,\text{jet}}^{\text{det,ch}} \right) \times R_{\text{instr}} \left(p_{T,\text{jet}}^{\text{det,ch}}, p_{T,\text{jet}}^{\text{part,ch}} \right). \quad (12)$$

Equation 11 is then approximately inverted using regularized unfolding methods [98, 99]. We utilize Singular Value Decomposition (SVD) [98] and Iterative Bayesian unfolding [99] as implemented in the RooUnfold package [100].

10.3.2 $p + p$ collisions

For $p + p$ collisions, uncorrelated background is negligible in the $p_{T,\text{jet}}$ -range considered in the analysis. Only corrections for the instrumental response therefore need to be unfolded; i.e. $R_{\text{total}} = R_{\text{instr}}$. Determination of R_{instr} is described in Sect. 10.1.1.

Iterative Bayesian unfolding is used for $p + p$ collisions. The unfolding is regularized by restricting the number of iterations to $n_{\text{iter}} = 4$ for $R = 0.2$ and $n_{\text{iter}} = 3$ for $R = 0.5$. These values were determined by the inflection point in the distribution of χ^2/NDF from comparison of the backfolded distribution and the raw data, and adding one iteration. The prior distributions used in the unfolding correspond to the π^0 -triggered recoil-jet distributions from the simulation described in Sect. 10.1.1.

10.3.3 Au + Au collisions

Figure 17, bottom panel, shows the combined response matrix for π^0 -triggered central Au + Au collisions. Prior distributions correspond to π^0 -triggered and

γ_{dir} -triggered recoil-jet distributions generated by PYTHIA, modified by suppression of the recoil-jet yield to account for jet quenching [49].

For Iterative Bayesian unfolding, regularization corresponds to truncation of the number of iterations at values between 2 and 5. SVD unfolding is regularized by truncating the expansion at a value of the stabilization term (k). This value is varied in the range 2-4, and is optimized using the value of χ^2/NDF from comparing the unfolded distribution multiplied by R_{total} (“backfolding”, analogous to Eq. 11) with the measured distribution M .

The $p_{\text{T,jet}}^{\text{reco,ch}}$ distributions after ME subtraction (Fig. 9) constitute the input distributions for unfolding. The distributions for $R = 0.2$ drop rapidly in the region $p_{\text{T,jet}}^{\text{reco,ch}} < 0$, and the full distribution is used. However, for $R = 0.5$ the subtracted distributions extend to $p_{\text{T,jet}}^{\text{reco,ch}} < -10$ GeV/ c , with data points that oscillate around zero with large variance (note that negative values are not shown in Fig. 9, due to the logarithmic vertical axis).

The region $p_{\text{T,jet}}^{\text{reco,ch}} < 0$ of the $R = 0.5$ distributions therefore has limited information content, and inclusion of that range gives unstable unfolding results. Unfolding for $R = 0.5$ therefore only utilizes data from the distributions in Fig. 9 for $p_{\text{T,jet}}^{\text{reco,ch}} > 0$.

11 Systematic uncertainties

Systematic uncertainties are determined following the procedures in Ref. [49, 58]. The components of the systematic uncertainty are as follows:

- instrumental effects: uncertainty in tracking efficiency and resolution;
- unfolding: uncertainty due to choice of regularization, prior, and algorithm;
- uncorrelated background yield, Au+Au collisions: uncertainty in boundary of normalization region for measuring f^{ME} ;
- γ_{dir} purity: uncertainty in measured value of R_{impurity} (Eq. 8);
- fragmentation model: variation in choice of Monte-Carlo model used to calculate the response matrix and jet-matching efficiency.

For each source of uncertainty, alternative unfolding solutions are generated by varying the corresponding parameter or algorithm. The variation

with the largest relative difference to the baseline solution is assigned as the systematic uncertainty for that source. Variants whose unfolding does not converge or which produces anomalously large χ^2/NDF between the back-folded solution and the raw data are excluded.

11.1 $p + p$ collisions

The specific variations are as follows:

- For the unfolding uncertainty, n_{iter} is varied ± 1 relative to its baseline value. Several Lévy functions are used as alternative priors.
- For γ_{dir} -triggered distributions, R_{impurity} is varied within its measured uncertainties (see Sect. 8). Near the limit of the kinematic range for jets recoiling from γ_{dir} triggers, the uncertainty on the recoil-jet yields can be very large, as the yields can be consistent with zero.
- For the instrumental uncertainty, an alternative unfolding procedure is carried out in which R_{instr} is constructed from π^0 -triggered recoil-jet spectra generated by PYTHIA 8.185, with a parameterized instrumental response applied. The resulting matrix R_{instr} is used to unfold the γ_{dir} - and π^0 -triggered recoil-jet distributions.
- Tracking efficiency in the parameterized instrumental response is varied by $\pm 4\%$ (absolute).
- Tracking resolution in the parameterized instrumental response is quantified by a polynomial fit to the ratio of the difference between reconstructed track p_{T} and matched particle-level p_{T} over the matched particle-level p_{T} . An alternative fit to the resolution is used as systematic variation.
- The fragmentation model for the calculation of R_{instr} is varied by using γ_{dir} -triggered events generated by HERWIG-7 for $p + p$ collisions at $\sqrt{s} = 200$ GeV with the default tune [101]. The difference between PYTHIA and HERWIG-derived corrections, which are found to be independent of $E_{\text{T}}^{\text{trig}}$, is assigned as the fragmentation model uncertainty. For $R = 0.2$ the uncertainty is negligible for the full measured range of $p_{\text{T,jet}}$. For $R = 0.5$, the uncertainty is 15% at $p_{\text{T,jet}} = 3$ GeV/ c , 6% at $p_{\text{T,jet}} = 5$ GeV/ c , and negligible for $p_{\text{T,jet}} > 6$ GeV/ c .

Table 4: Significant systematic uncertainties for π^0 triggers in $p + p$ collisions. The cumulative uncertainty is the sum in quadrature of the individual contributions.

$p + p$; Trigger: π^0					
E_T^{trig} [GeV]	R	$p_{T,\text{jet}}$ [GeV/ c]	Systematic uncertainty (%)		
			instr	unfold	cumulative
[9,11]	0.2	[5,10]	7	2	7
		[10,15]	9	2	9
		[15,20]	12	4	12
	0.5	[5,10]	6	4	8
		[10,15]	10	4	11
		[15,20]	14	7	16
[11,15]	0.2	[5,10]	7	1	7
		[10,15]	8	2	8
		[15,20]	10	3	11
	0.5	[5,10]	5	5	8
		[10,15]	9	5	10
		[15,20]	11	9	14

Tables 4 and 5 show the largest systematic uncertainties for $p + p$ collisions. The cumulative systematic uncertainty of the recoil-jet yield is the quadrature sum of uncertainties from each component.

11.2 Au + Au collisions

The uncertainty associated with the tracking efficiency is assessed by varying the absolute efficiency by $\pm 4\%$. Corrections for the track p_T -resolution and weak decays are found to be significantly smaller than those associated with the tracking efficiency, consistent with Ref. [49]. No systematic uncertainty due to the p_T -resolution or weak decays is assigned.

The uncertainty due to the choice of unfolding algorithm was assessed by comparing the results of the SVD algorithm to the alternative Iterative Bayesian algorithm. Uncertainty due to the choice of prior was determined by using a modified PYTHIA-generated prior (Sect. 10.3.3) and a Levy function [49]). The uncertainty associated with the choice of regularization for SVD unfolding was assessed by varying the value of $k_{\text{reg}} \pm 1$ relative to the default value. Varying the choice of regularization for Iterative Bayesian

Table 5: Significant systematic uncertainties for γ_{dir} triggers in $p + p$ collisions. The cumulative uncertainty is the sum in quadrature of the individual contributions.

$p + p$; Trigger: γ_{dir}						
$E_{\text{T}}^{\text{trig}}$ [GeV]	R	$p_{\text{T,jet}}$ [GeV/ c]	Systematic uncertainty (%)			
			instr	unfold	purity	cumulative
[9,11]	0.2	[5,10]	11	2	80	81
	0.5	[5,10]	14	15	81	83
[11,15]	0.2	[5,10]	9	2	21	23
		[10,15]	17	101	100	143
	0.5	[5,10]	7	8	2	10
		[10,15]	12	12	16	23
[15,20]	0.2	[5,10]	3	2	13	14
		[10,15]	2	16	2	17
		[15,20]	8	13	15	21
	0.5	[5,10]	4	2	12	13
		[10,15]	3	2	12	16
		[15,20]	2	6	15	16

unfolding generates negligible change.

Table 2 and Figs. 7 and 8 show the nominal f^{ME} normalization regions. To assess the uncertainty associated with this choice, the upper limit of this region was varied by 1 GeV/ c .

The value of R_{impurity} is determined from the near-side correlation yields of π^0 vs. γ_{rich} triggers (Sect. 8). The systematic uncertainty in R_{impurity} is estimated by varying the range of $z_{\text{T}} = p_{\text{T,track}}/E_{\text{T}}^{\text{trig}}$ of the tracks counted in the near-side correlation measurement [58]. By varying R_{impurity} within its uncertainty, the corresponding uncertainty on the recoil-jet yields is determined.

The effects of varying the fragmentation model used to determine R_{instr} for central Au + Au collisions were studied in Ref. [49], and were found to be small relative to other systematic effects. We therefore do not consider this contribution further here for central Au + Au measurements.

Tables 6 and 7 show the systematic uncertainties for central Au + Au collisions. The cumulative systematic uncertainty in the recoil-jet yield is the quadrature sum of the uncertainties from each individual source.

Table 6: Significant systematic uncertainties for π^0 triggers in central Au+Au collisions. Cumulative uncertainty is the quadrature sum of the individual contributions.

Central Au + Au; Trigger: π^0							
E_T^{trig} [GeV]	R	$p_{T,\text{jet}}$ [GeV/ c]	Systematic uncertainty (%)				
			instr	unfold	ME norm	δp_T	cumulative
[9,11]	0.2	[5,10]	4	11	17	18	27
		[10,15]	5	20	2	9	22
		[15,20]	5	22	4	13	26
	0.5	[5,10]	3	34	7	5	35
		[10,15]	7	36	2	4	36
		[15,20]	8	24	2	9	26
[11,15]	0.2	[5,10]	4	36	14	10	40
		[10,15]	5	29	8	11	32
		[15,20]	5	38	7	7	39
	0.5	[5,10]	6	38	4	6	39
		[10,15]	8	29	3	3	30
		[15,20]	8	22	2	7	24

Table 7: Significant systematic uncertainties for γ_{dir} triggers in central Au + Au collisions. Cumulative uncertainty is the quadrature sum the individual contributions.

Central Au + Au; Trigger: γ_{dir}								
E_T^{trig} [GeV]	R	$p_{T,\text{jet}}$ [GeV/ c]	Systematic uncertainty (%)					
			instr	unfold	ME norm	δp_T	purity	cumulative
[9,11]	0.2	[5,10]	4	30	18	14	12	40
	0.5	[5,10]	5	30	16	3	5	34
[11,15]	0.2	[5,10]	4	36	17	10	3	41
		[10,15]	5	20	10	15	16	31
	0.5	[5,10]	2	36	10	8	2	38
		[10,15]	5	20	11	3	11	26
[15,20]	0.2	[5,10]	4	26	12	11	10	32
		[10,15]	5	32	11	10	23	42
	0.5	[5,10]	3	44	12	9	5	46
		[10,15]	4	42	10	6	9	44

12 Closure test

A closure test is used to validate the analysis algorithm. The test is based on detector-level events which are embedded into real data to model the effects of uncorrelated background and then subject to the full analysis chain that is used for the real data analysis, including unfolding and estimation of systematic uncertainties. Corrected distributions from these fully analysed events are then compared to those from the initial particle-level events (“Truth”). Successful closure corresponds to the agreement of these two distributions within uncertainties.

12.1 $p + p$ collisions

The $p + p$ closure test was carried out using events generated by PYTHIA 6.426 Perugia 0 tune for $p + p$ collisions at $\sqrt{s} = 200$ GeV, selected by a di-jet trigger condition. Detector-level events from this population are embedded into STAR 2009 zero-bias $p + p$ data (hybrid events). Jets are reconstructed in the same manner as data using both the particle-level and detector-level hybrid events. The detector-level recoil-jet distributions are modified to correspond to the trigger statistics of the measured data.

The detector-level event population is divided into two sub-samples of roughly equal size. These sub-samples correspond to the two orientations of the STAR magnetic field in which data were taken: Full-Field (FF) and Reverse Full-Field (RFF). The closure test utilizes the RFF sub-sample for calculating R_{total} and the FF sub-sample serving as pseudo-data for validation. Jet reconstruction, unfolding, and determination of systematic uncertainties, are carried on the RFF sub-sample in the same way as is done for real data.

Figure 18 shows corrected distributions for π^0 -triggered events with $9 < E_{\text{T}}^{\text{trig}} < 11$ GeV and recoil jets with $R = 0.2$ and 0.5 , compared to the corresponding Truth (particle-level) distributions whose statistical errors have been modified to match the systematic precision of the data. The unfolded and Truth distributions agree within the systematic precision of the measurement, thereby validating the $p + p$ analysis chain for this choice of kinematics. Similarly good closure is observed for triggers with $11 < E_{\text{T}}^{\text{trig}} < 15$ and $15 < E_{\text{T}}^{\text{trig}} < 20$ GeV, and with the roles of the FF and RFF data sub-samples reversed. This closure study validates the $p + p$ analysis chain over the full reported kinematic range.

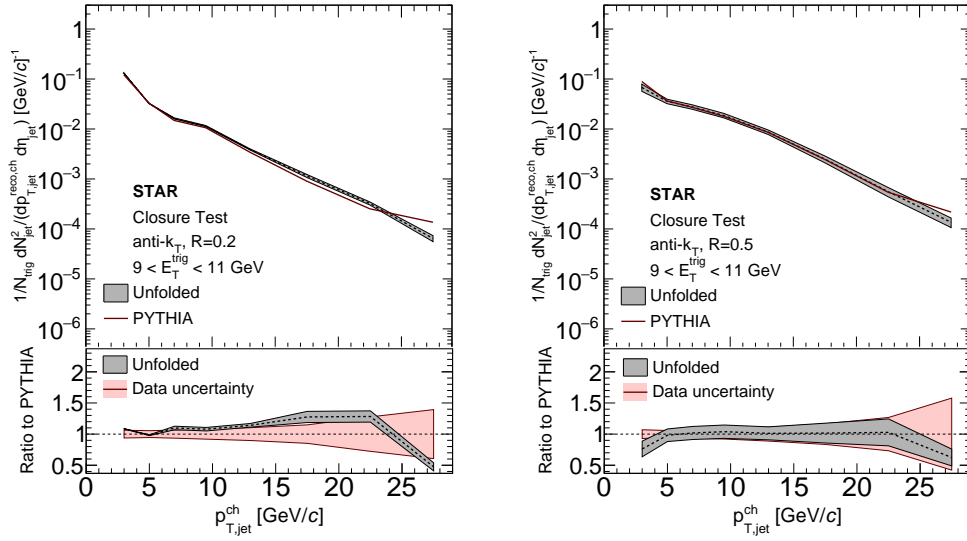


Figure 18: Closure test for $p + p$ collisions: π^0 -triggered events with $9 < E_T^{\text{trig}} < 11$ GeV; recoil jets with $R = 0.2$ (left) and 0.5 (right). Upper panel: semi-inclusive recoil-jet distributions. Dotted line shows unfolded detector-level distribution. Band on unfolded detector-level represents systematic uncertainty. Red line shows particle-level jet distribution. Band on particle-level represents systematic precision of the data. Lower panel: ratio of unfolded detector- and particle-level distributions.

12.2 Au + Au collisions

The closure test for central Au + Au collisions utilizes PYTHIA-generated events for $p + p$ collisions at $\sqrt{s} = 200$ GeV which contain a π^0 trigger in the range $9 < E_T^{\text{trig}} < 11$ GeV. The trigger statistics are the same as those of the real data. Detector-level events are generated with the same fast simulation approach used in Sect. 10.1.2 and are embedded in central Au+Au events recorded with a MB trigger. The full analysis chain is then applied to these hybrid events, including jet reconstruction, subtraction of ME, and corrections. Systematic uncertainties are determined by the same procedures as used for real data.

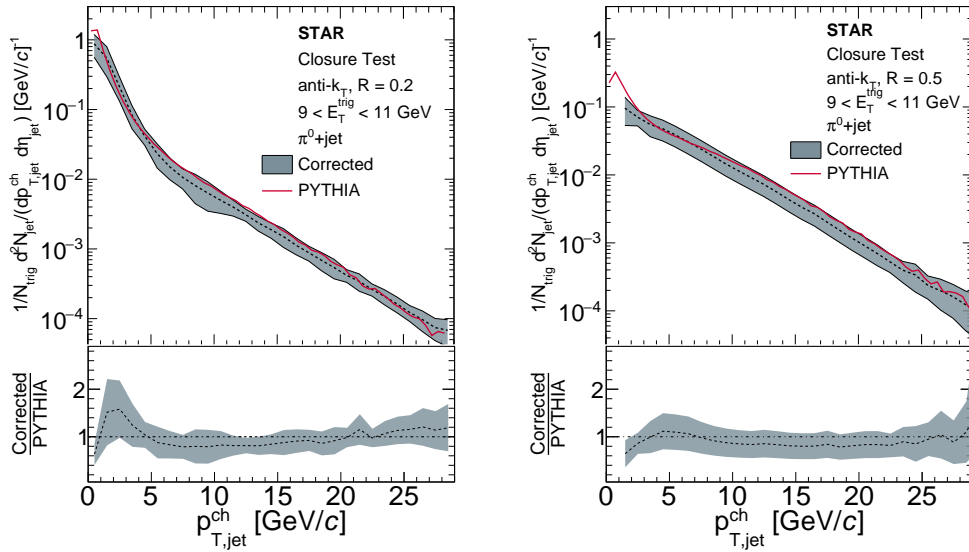


Figure 19: Closure test for central Au + Au collisions: π^0 -triggered events with $9 < E_T^{\text{trig}} < 11$ GeV; recoil jets with $R = 0.2$ (left) and 0.5 (right). Upper panel: semi-inclusive recoil-jet distributions. Red line shows PYTHIA truth distribution (particle-level). Lower panel: ratio of data and PYTHIA truth distributions.

Figure 19 shows corrected semi-inclusive recoil-jet distributions for such hybrid events, for $R = 0.2$ and 0.5 . The ratio of corrected data to the PYTHIA truth distributions in the lower panel is consistent with unity within the systematic uncertainty, over the full reported range of $p_{T,\text{jet}}^{\text{ch}}$. This agreement, corresponding to closure, validates the analysis chain for central

Au + Au collisions.

13 Results

This section compares fully-corrected distributions measured in $p + p$ and central Au + Au collisions using the observables defined in Sect. 4.3. Comparisons of these results to theoretical calculations are presented in the companion Letter [59].

13.1 Corrected recoil $p_{T,\text{jet}}^{\text{ch}}$ distributions

Figure 20 shows fully-corrected $p_{T,\text{jet}}^{\text{ch}}$ distributions for recoil jets with $R = 0.2$ and 0.5 , in γ_{dir} -triggered and π^0 -triggered $p + p$ collisions at $\sqrt{s} = 200$ GeV. The distributions are shown as continuous bands rather than distinct points, to indicate the strong off-diagonal covariance of the systematic uncertainty [49]. Higher $E_{\text{T}}^{\text{trig}}$ corresponds to a harder recoil-jet spectrum, as expected. PYTHIA-6 STAR tune calculations are also shown. For $R = 0.2$, PYTHIA largely reproduces the measured distributions within $\sim 30\%$, except the γ_{dir} -triggered data for $15 < E_{\text{T}}^{\text{trig}} < 20$ GeV. For $R = 0.5$, PYTHIA reproduces the data except for π^0 triggers in $11 < E_{\text{T}}^{\text{trig}} < 15$ GeV.

Figure 21 shows the same distributions for Au + Au collisions at $\sqrt{s_{\text{NN}}} = 200$ GeV. An ordering of the recoil spectra as a function of $E_{\text{T}}^{\text{trig}}$ is likewise observed, which is qualitatively similar to that for $p + p$ collisions in Fig. 20.

The recoil-jet spectra extend to larger $p_{T,\text{jet}}^{\text{ch}}$ for π^0 than for γ_{dir} triggers, as expected, due to the stronger constraint on kinematic balance for γ_{dir} triggers. The π^0 -triggered spectra for $15 < E_{\text{T}}^{\text{trig}} < 20$ GeV are not shown, due to their limited statistical precision arising from the stringent TSP cut required for high π^0 purity (Fig. 2). While the π^0 -triggered distributions in this $E_{\text{T}}^{\text{trig}}$ selection are sufficient for the background subtraction needed to obtain the γ_{dir} -triggered distributions, they are not precise enough for good convergence of the unfolding to obtain corrected π^0 -triggered spectra.

13.2 Recoil-jet yield modification: I_{AA}

Figure 22 shows I_{AA} (Eq. 3) as a function of $p_{T,\text{jet}}^{\text{ch}}$ for γ_{dir} - and π^0 -triggered recoil jet distributions. For $R = 0.2$, I_{AA} in all cases decreases with increasing $p_{T,\text{jet}}^{\text{ch}}$ for $p_{T,\text{jet}}^{\text{ch}} < 10$ GeV/ c and is significantly below unity for $p_{T,\text{jet}}^{\text{ch}} > 10$

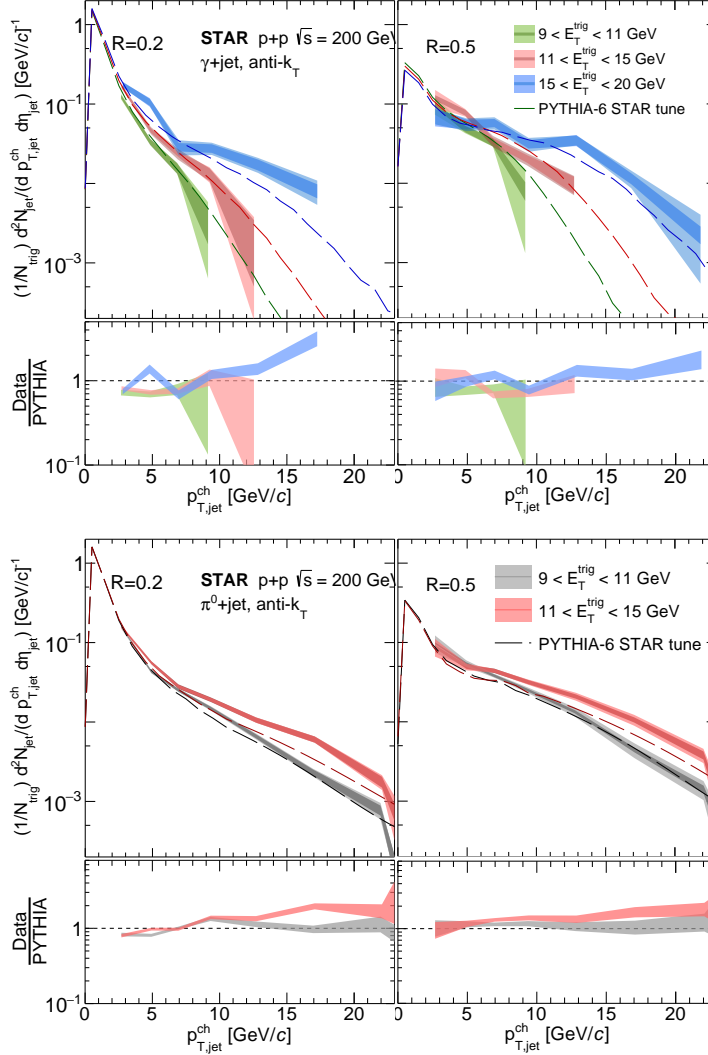


Figure 20: Corrected semi-inclusive charged-particle recoil-jet distributions for γ_{dir} -triggered (upper) and π^0 -triggered (lower) $p + p$ collisions at $\sqrt{s} = 200$ GeV, in E_T^{trig} bins. Left: $R = 0.2$; right: $R = 0.5$. Dark bands are statistical error; light bands are systematic uncertainty. The ratios in the lower sub-panels show the systematic uncertainties only. Dashed lines show the distribution from PYTHIA-6 STAR tune.

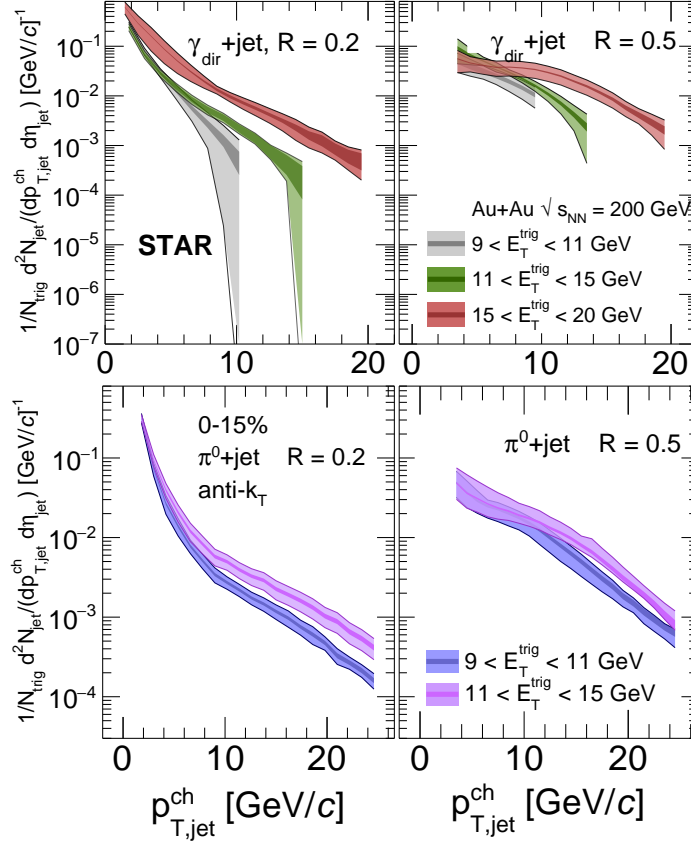


Figure 21: Corrected semi-inclusive charged-particle recoil-jet distributions for γ_{dir} -triggered (upper) and π^0 -triggered (lower) Au + Au collisions at $\sqrt{s_{\text{NN}}} = 200 \text{ GeV}$, in E_T^{trig} bins. Left: $R = 0.2$; right: $R = 0.5$. Dark bands are statistical error; light bands are systematic uncertainty.

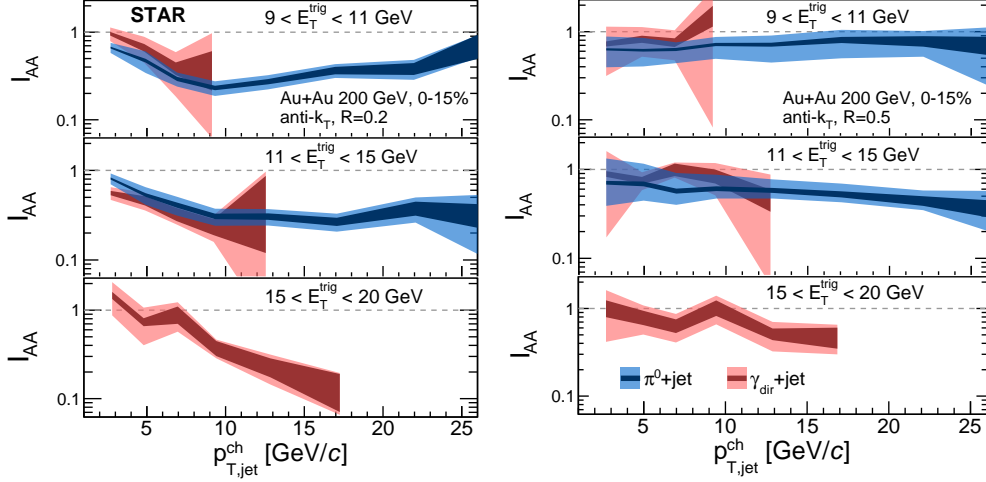


Figure 22: I_{AA} for γ_{dir} - and π^0 -triggered recoil jet distributions measured in $p + p$ (Fig. 20) and central Au + Au collisions (Fig. 21) at $\sqrt{s_{NN}} = 200$ GeV. Left: $R = 0.2$; right: $R = 0.5$. Top: $9 < E_T^{\text{trig}} < 11$ GeV; middle: $11 < E_T^{\text{trig}} < 15$ GeV; bottom: $15 < E_T^{\text{trig}} < 20$ GeV.

GeV/ c indicating medium-induced jet energy loss. For $R = 0.5$, I_{AA} in all cases is closer to unity for $p_{T,\text{jet}}^{\text{ch}} > 10$ GeV/ c . These features suggest that the energy and momentum that are lost by small- R jets at high $p_{T,\text{jet}}^{\text{ch}}$ due to jet quenching may be recovered at both large angles to the jet axis by large- R jets, and at low $p_{T,\text{jet}}^{\text{ch}}$ by small- R jets.

For both $9 < E_T^{\text{trig}} < 11$ and $11 < E_T^{\text{trig}} < 15$ GeV, and for both $R = 0.2$ and 0.5 , the γ_{dir} -triggered and π^0 -triggered I_{AA} distributions are consistent within uncertainties. This is notable in light of the differences expected in the recoil-jet populations in terms of quark/gluon fraction and path-length distribution (Sect. 4.1). However, the magnitude of medium-induced yield suppression measured by I_{AA} depends upon both the population-averaged energy loss and the shape of the recoil-jet spectrum. Figures 20 and 21 show that the recoil-jet spectrum is steeper for γ_{dir} than for π^0 triggers in the same E_T^{trig} bin, which suggests larger energy loss on average for the π^0 -triggered recoil-jet population. The companion Letter [59] further explores this question using comparison to theoretical model calculations.

13.3 Jet shape modification: $\mathfrak{R}^{0.2/0.5}$

The observable $\mathfrak{R}^{\frac{\text{small-}R}{\text{large-}R}}$ (Eq. 4) probes the transverse profile of jet energy. Figure 23 shows distributions of $\mathfrak{R}^{0.2/0.5}$ measured for π^0 and γ_{dir} triggers in $p + p$ and central Au + Au collisions. The systematic uncertainty in the ratio takes into account the correlated uncertainties in numerator and denominator. The systematic uncertainty due to instrumental effects largely cancels in the ratio.

For $p + p$ collisions, $\mathfrak{R}^{0.2/0.5}$ is less than unity for $p_{\text{T,jet}}^{\text{ch}} \gtrsim 7 \text{ GeV}/c$, reflecting the transverse energy profile of jets in vacuum. Figure 23 also shows distributions of $\mathfrak{R}^{0.2/0.5}$ calculated by PYTHIA-6 STAR tune for $p + p$ collisions, which are consistent within uncertainties with the data. Similar level of agreement with data has been found for QCD and model calculations of $\mathfrak{R}^{0.2/0.5}$ in $p + p$ collisions for inclusive jet production [89–92, 102], and semi-inclusive recoil-jet yields [40].

Note that the shape of the $\mathfrak{R}^{0.2/0.5}$ distribution in $p + p$ collisions differs markedly at low $p_{\text{T,jet}}^{\text{ch}}$ for inclusive jet cross sections compared to semi-inclusive yields. For inclusive jet cross sections, $\mathfrak{R}^{\frac{\text{small-}R}{\text{large-}R}}$ decreases as $p_{\text{T,jet}}$ decreases [91, 92, 102], consistent with the well-established broadening of the transverse jet profile for jets at low $p_{\text{T,jet}}$, whereas for semi-inclusive distributions, Fig. 23 shows that $\mathfrak{R}^{0.2/0.5}$ increases as $p_{\text{T,jet}}^{\text{ch}}$ decreases.

As seen in the figure, the PYTHIA-6 STAR tune calculation reproduces this trend well; QCD calculations and PYTHIA-6 likewise reproduce well the opposite trend for inclusive cross sections [91, 102]. We therefore explore whether these features can be accounted for by elementary QCD processes, focussing on $\mathfrak{R}^{0.2/0.5}$ for π^0 -triggered data; similar considerations apply to γ_{dir} -triggered data. In this case, the π^0 trigger is a leading fragment of the “trigger jet,” which is not measured in the analysis. However, $p_{\text{T,jet}}^{\text{ch}}$ of the trigger jet is necessarily larger than $p_{\text{T}}^{\text{trig}}$ of the trigger π^0 . In a LO picture, in which jet production is a $2 \rightarrow 2$ process, the recoil jet must therefore also have a value of $p_{\text{T,jet}}^{\text{ch}}$ that is larger than $p_{\text{T}}^{\text{trig}}$.

We therefore introduce a new observable,

$$\tilde{z} = \frac{p_{\text{T}}^{\text{trig}}}{p_{\text{T,jet}}^{\text{ch}}}, \quad (13)$$

which is the ratio of p_{T} of the π^0 trigger to $p_{\text{T,jet}}^{\text{ch}}$ of the recoil jet. In the absence of initial- k_{T} smearing effects, and accounting for the fact that the

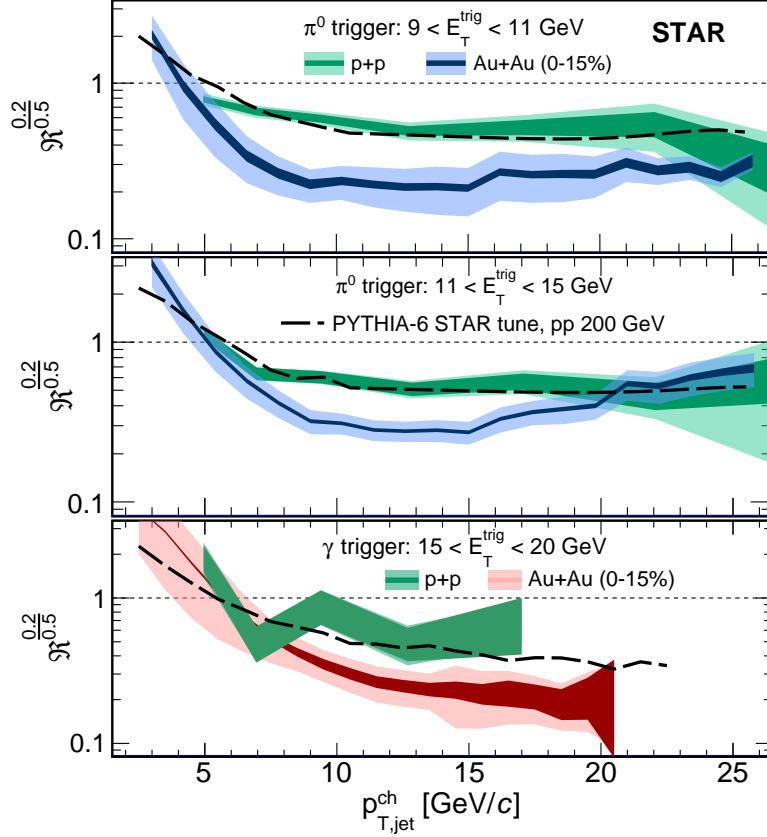


Figure 23: Recoil-jet yield ratio $\mathfrak{R}_{\text{large}-R}^{\text{small}-R}$ for $R = 0.2$ and 0.5 measured in $p + p$ and $\text{Au} + \text{Au}$ collisions. Top panel: π^0 trigger, $9 < E_T^{\text{trig}} < 11$ GeV; middle panel: π^0 trigger, $11 < E_T^{\text{trig}} < 15$ GeV; bottom panel: γ_{dir} trigger, $15 < E_T^{\text{trig}} < 20$ GeV. Dark bands are statistical error; light bands are systematic uncertainty. Also shown are the same distributions calculated using PYTHIA-6 STAR tune for $p + p$ collisions.

recoil jet is measured only with charged particles, LO production corresponds predominantly to $\tilde{z} < 1.5$.

However, Fig. 23 shows that the increase in $\mathfrak{R}^{0.2/0.5}$ as $p_{T,\text{jet}}^{\text{ch}}$ decreases occurs predominantly in the region $\tilde{z} > 1.5$, where LO production is suppressed. Production processes at higher order include gluon radiation at significant angles to the jet axis. For radiation at angles between ~ 0.2 and ~ 0.5 radians, jet reconstruction with $R = 0.2$ may find two separate jets while jet reconstruction with $R = 0.5$ finds only one.

These elements together may account for the increase in $\mathfrak{R}^{0.2/0.5}$ towards low $p_{T,\text{jet}}^{\text{ch}}$ for $p + p$ collisions: in the region $\tilde{z} > 1.5$, the energy profile of recoil jets for this semi-inclusive selection is broader than that of the inclusive jet population at the same value of $p_{T,\text{jet}}^{\text{ch}}$, and is therefore more frequently split into two jets by jet reconstruction with $R = 0.2$ than for $R = 0.5$. Note that the semi-inclusive analysis approach counts all correlated jet yield in the recoil acceptance, so that this effect corresponds to a growth in $\mathfrak{R}^{0.2/0.5}$, as observed.

Validation of this picture can be carried out using QCD calculations which exhibit the same features, and by additional jet substructure measurements, both of which are beyond the scope of this paper. If validated, this mechanism can potentially be used to generate a population of initially “wide jets” in heavy-ion collisions, in order to explore the interplay between jet substructure and jet quenching [103].

Figure 23 shows that for central Au+Au collisions, $\mathfrak{R}^{0.2/0.5}$ is additionally suppressed relative to its value for $p + p$ collisions for π^0 triggers in the range $7 < p_{T,\text{jet}}^{\text{ch}} < 20$ GeV/ c , and for γ_{dir} triggers in the range $p_{T,\text{jet}}^{\text{ch}} > 8$ GeV/ c . This additional suppression corresponds to medium-induced jet broadening. This observation of intra-jet broadening, combined with the measurement of I_{AA} values close to unity for $R = 0.5$ (Fig. 22), suggests that the typical angular scale of medium-induced energy momentum transfer due to jet quenching is less than 0.5 radians. This topic is explored in detail in the companion Letter [59].

13.4 Comparison with previous results

This section compares π^0 -triggered measurements from this analysis with previously published measurements of h +jet correlations in Au + Au collisions at $\sqrt{s_{\text{NN}}} = 200$ GeV [49]. These analyses differ in their choice of centrality, trigger, and reference spectrum for measuring yield suppression. Neverthe-

less, they address similar physics questions, and such differences may have only secondary effect on the physics results. This comparison provides a cross-check of the two analyses.

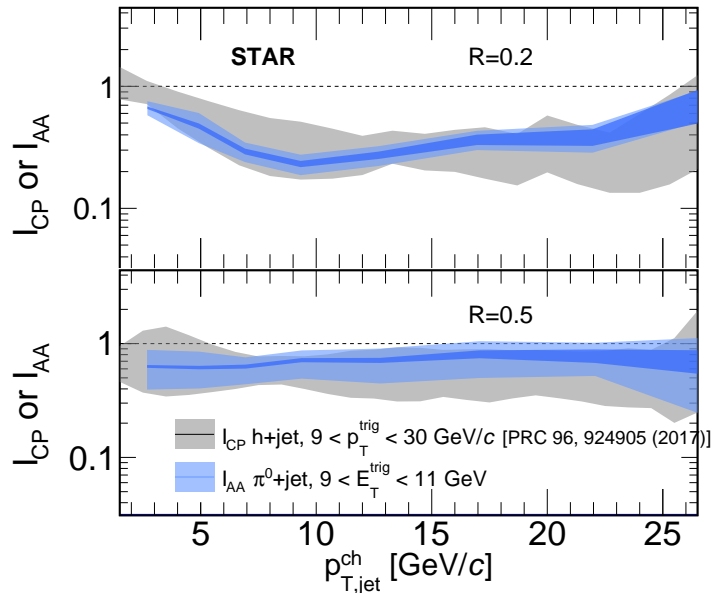


Figure 24: Comparison of I_{AA} from π^0 -triggered distributions in this analysis with I_{CP} from hadron-triggered distributions [49], for $R=0.2$ (upper) and 0.5 (lower).

Figure 24 compares the π^0 -triggered distribution of I_{AA} with I_{CP} (ratio of recoil-jet distributions in central and peripheral Au + Au collisions) from Ref. [49], for $R = 0.2$ and 0.5 , while Fig. 25 compares the ratio $\mathfrak{R}_{\frac{\text{small}-R}{\text{large}-R}}$ with $R = 0.2$ and $R = 0.5$ in the two analyses. The systematic uncertainty and statistical error are significantly smaller in this analysis, for both observables. The two analyses are consistent within uncertainties.

14 Summary

We have reported the first measurement of semi-inclusive distributions of charged-particle jets recoiling from γ_{dir} and π^0 triggers in $p + p$ and central

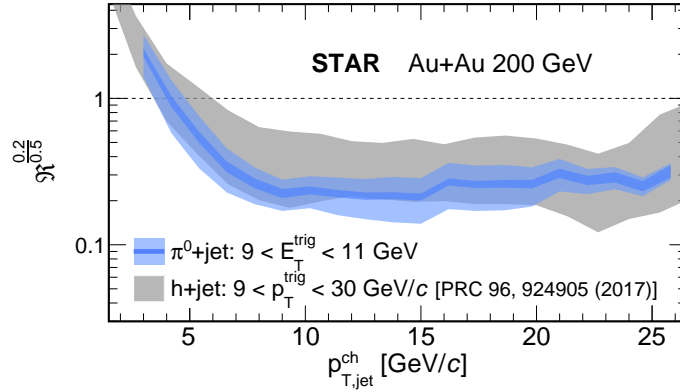


Figure 25: Same as Fig. 24 for $\mathfrak{R}^{\frac{\text{small}-R}{\text{large}-R}}$ with $R = 0.2$ and $R = 0.5$.

Au + Au collisions at $\sqrt{s_{\text{NN}}} = 200$ GeV. Fully-corrected recoil-jet distributions are measured for $R = 0.2$ and 0.5 , with $9 < E_{\text{T}}^{\text{trig}} < 20$ GeV. The measurements are consistent with results in a previous publication that utilized charged-hadron triggers in central and peripheral Au + Au collisions, with significantly improved uncertainties.

Recoil-yield suppression is observed in the range $p_{\text{T,jet}}^{\text{ch}} > 10$ GeV/c for $R = 0.2$, with the magnitude of suppression consistent within uncertainties for π^0 and γ_{dir} -triggered data. Significantly less suppression is observed for $R = 0.5$, and at low $p_{\text{T,jet}}^{\text{ch}}$ for both $R = 0.2$ and 0.5 .

The transverse structure of jets and its in-medium modification is measured using $\mathfrak{R}^{0.2/0.5}$, the ratio of semi-inclusive recoil-jet yields for $R = 0.2$ and 0.5 . The distribution of $\mathfrak{R}^{0.2/0.5}$ in $p + p$ collisions, which is well-reproduced by QCD calculations, exhibits low- $p_{\text{T,jet}}^{\text{ch}}$ behavior that is opposite to that of inclusive jet cross sections, suggesting that the semi-inclusive approach suppresses LO production processes for $p_{\text{T,jet}}^{\text{ch}} \ll E_{\text{T}}^{\text{trig}}$. The value of $\mathfrak{R}^{0.2/0.5}$ in Au + Au collisions is markedly suppressed relative to that in $p + p$ collisions, for both π^0 and γ_{dir} triggers and for $p_{\text{T,jet}}^{\text{ch}} > p_{\text{T}}^{\text{trig}}$, providing a new measurement of medium-induced jet broadening at RHIC energies and its angular scale.

15 Acknowledgments

Acknowledgments- We thank Shanshan Cao, Tan Luo, Guang-You Qin, Abhijit Majumder, Daniel Pablos, Krishna Rajagopal, Chathuranga Sirimanna, Xin-Nian Wang, and Ivan Vitev for providing theoretical calculations. We thank the RHIC Operations Group and RCF at BNL, the NERSC Center at LBNL, and the Open Science Grid consortium for providing resources and support. This work was supported in part by the Office of Nuclear Physics within the U.S. DOE Office of Science, the U.S. National Science Foundation, National Natural Science Foundation of China, Chinese Academy of Science, the Ministry of Science and Technology of China and the Chinese Ministry of Education, the Higher Education Sprout Project by Ministry of Education at NCKU, the National Research Foundation of Korea, Czech Science Foundation and Ministry of Education, Youth and Sports of the Czech Republic, Hungarian National Research, Development and Innovation Office, New National Excellency Programme of the Hungarian Ministry of Human Capacities, Department of Atomic Energy and Department of Science and Technology of the Government of India, the National Science Centre and WUT ID-UB of Poland, the Ministry of Science, Education and Sports of the Republic of Croatia, German Bundesministerium für Bildung, Wissenschaft, Forschung and Technologie (BMBF), Helmholtz Association, Ministry of Education, Culture, Sports, Science, and Technology (MEXT) and Japan Society for the Promotion of Science (JSPS).

References

- [1] W. Busza, K. Rajagopal, and W. van der Schee, “Heavy Ion Collisions: The Big Picture, and the Big Questions,” [Ann. Rev. Nucl. Part. Sci. **68** \(2018\) 339–376](#), [arXiv:1802.04801 \[hep-ph\]](#).
- [2] J. W. Harris and B. Müller, ““QGP Signatures” Revisited,” [arXiv:2308.05743 \[hep-ph\]](#).
- [3] U. Heinz and R. Snellings, “Collective flow and viscosity in relativistic heavy-ion collisions,” [Ann. Rev. Nucl. Part. Sci. **63** \(2013\) 123–151](#), [arXiv:1301.2826 \[nucl-th\]](#).
- [4] **JETSCAPE** Collaboration, D. Everett et al., “Multisystem Bayesian constraints on the transport coefficients of QCD matter,” [Phys. Rev. C **103** no. 5, \(2021\) 054904](#), [arXiv:2011.01430 \[hep-ph\]](#).
- [5] **JETSCAPE** Collaboration, D. Everett et al., “Phenomenological constraints on the transport properties of QCD matter with data-driven model averaging,” [Phys. Rev. Lett. **126** no. 24, \(2021\) 242301](#), [arXiv:2010.03928 \[hep-ph\]](#).
- [6] G. Nijs, W. van der Schee, U. Gürsoy, and R. Snellings, “Bayesian analysis of heavy ion collisions with the heavy ion computational framework Trajectum,” [Phys. Rev. C **103** no. 5, \(2021\) 054909](#), [arXiv:2010.15134 \[nucl-th\]](#).
- [7] L. Cunqueiro and A. M. Sickles, “Studying the QGP with Jets at the LHC and RHIC,” [Prog. Part. Nucl. Phys. **124** \(2022\) 103940](#), [arXiv:2110.14490 \[nucl-ex\]](#).
- [8] M. Cacciari, G. P. Salam, and G. Soyez, “FastJet User Manual,” [Eur. Phys. J. C **72** \(2012\) 1896](#), [arXiv:1111.6097 \[hep-ph\]](#).
- [9] **STAR** Collaboration, B. I. Abelev et al., “Longitudinal double-spin asymmetry and cross section for inclusive jet production in polarized proton collisions at $\sqrt{s} = 200$ GeV,” [Phys. Rev. Lett. **97** \(2006\) 252001](#), [arXiv:hep-ex/0608030](#).
- [10] **STAR** Collaboration, L. Adamczyk et al., “Measurement of the cross section and longitudinal double-spin asymmetry for di-jet production

- in polarized pp collisions at $\sqrt{s} = 200$ GeV,” [Phys. Rev. D](#) **95** no. 7, (2017) 071103, [arXiv:1610.06616](#) [[hep-ex](#)].
- [11] **ALICE** Collaboration, B. Abelev et al., “Measurement of the inclusive differential jet cross section in pp collisions at $\sqrt{s} = 2.76$ TeV,” [Phys. Lett. B](#) **722** (2013) 262–272, [arXiv:1301.3475](#) [[nucl-ex](#)].
- [12] **ALICE** Collaboration, S. Acharya et al., “Measurements of inclusive jet spectra in pp and central Pb-Pb collisions at $\sqrt{s_{NN}} = 5.02$ TeV,” [Phys. Rev. C](#) **101** no. 3, (2020) 034911, [arXiv:1909.09718](#) [[nucl-ex](#)].
- [13] **ATLAS** Collaboration, G. Aad et al., “Measurement of the inclusive jet cross-section in proton-proton collisions at $\sqrt{s} = 7$ TeV using 4.5 invfb of data with the ATLAS detector,” [JHEP](#) **02** (2015) 153, [arXiv:1410.8857](#) [[hep-ex](#)]. [Erratum: [JHEP](#) 09, 141 (2015)].
- [14] **CMS** Collaboration, V. Khachatryan et al., “Measurement and QCD analysis of double-differential inclusive jet cross sections in pp collisions at $\sqrt{s} = 8$ TeV and cross section ratios to 2.76 and 7 TeV,” [JHEP](#) **03** (2017) 156, [arXiv:1609.05331](#) [[hep-ex](#)].
- [15] A. Majumder and M. Van Leeuwen, “The Theory and Phenomenology of Perturbative QCD Based Jet Quenching,” [Prog. Part. Nucl. Phys.](#) **66** (2011) 41–92, [arXiv:1002.2206](#) [[hep-ph](#)].
- [16] J. D. Bjorken, “Energy Loss of Energetic Partons in Quark - Gluon Plasma: Possible Extinction of High p_T Jets in Hadron - Hadron Collisions,” 8, 1982.
- [17] X.-N. Wang, M. Gyulassy, and M. Plumer, “The LPM effect in QCD and radiative energy loss in a quark gluon plasma,” [Phys. Rev. D](#) **51** (1995) 3436–3446, [arXiv:hep-ph/9408344](#).
- [18] R. Baier, Y. L. Dokshitzer, A. H. Mueller, and D. Schiff, “Radiative energy loss of high-energy partons traversing an expanding QCD plasma,” [Phys. Rev. C](#) **58** (1998) 1706–1713, [arXiv:hep-ph/9803473](#).

- [19] M. Gyulassy, P. Levai, and I. Vitev, “NonAbelian energy loss at finite opacity,” [*Phys. Rev. Lett.* **85** \(2000\) 5535–5538](#), [arXiv:nucl-th/0005032](#).
- [20] **STAR** Collaboration, C. Adler *et al.*, “Centrality dependence of high p_T hadron suppression in Au+Au collisions at $\sqrt{s_{NN}} = 130$ GeV,” [*Phys. Rev. Lett.* **89** \(2002\) 202301](#), [arXiv:nucl-ex/0206011](#).
- [21] **STAR** Collaboration, C. Adler *et al.*, “Disappearance of back-to-back high p_T hadron correlations in central Au+Au collisions at $\sqrt{s_{NN}} = 200$ GeV,” [*Phys. Rev. Lett.* **90** \(2003\) 082302](#), [arXiv:nucl-ex/0210033](#).
- [22] **STAR** Collaboration, J. Adams *et al.*, “Transverse momentum and collision energy dependence of high p_T hadron suppression in Au+Au collisions at ultrarelativistic energies,” [*Phys. Rev. Lett.* **91** \(2003\) 172302](#), [arXiv:nucl-ex/0305015](#).
- [23] **STAR** Collaboration, J. Adams *et al.*, “Direct observation of dijets in central Au+Au collisions at $\sqrt{s_{NN}} = 200$ GeV,” [*Phys. Rev. Lett.* **97** \(2006\) 162301](#), [arXiv:nucl-ex/0604018](#).
- [24] **STAR** Collaboration, L. Adamczyk *et al.*, “Jet-Hadron Correlations in $\sqrt{s_{NN}} = 200$ GeV $p + p$ and Central $Au + Au$ Collisions,” [*Phys. Rev. Lett.* **112** no. 12, \(2014\) 122301](#), [arXiv:1302.6184 \[nucl-ex\]](#).
- [25] **PHENIX** Collaboration, K. Adcox *et al.*, “Suppression of hadrons with large transverse momentum in central Au+Au collisions at $\sqrt{s_{NN}} = 130$ GeV,” [*Phys. Rev. Lett.* **88** \(2002\) 022301](#), [arXiv:nucl-ex/0109003](#).
- [26] **PHENIX** Collaboration, A. Adare *et al.*, “Neutral pion production with respect to centrality and reaction plane in Au+Au collisions at $\sqrt{s_{NN}}=200$ GeV,” [*Phys. Rev. C* **87** no. 3, \(2013\) 034911](#), [arXiv:1208.2254 \[nucl-ex\]](#).
- [27] **PHENIX** Collaboration, A. Adare *et al.*, “Transition in Yield and Azimuthal Shape Modification in Dihadron Correlations in Relativistic Heavy Ion Collisions,” [*Phys. Rev. Lett.* **104** \(2010\) 252301](#), [arXiv:1002.1077 \[nucl-ex\]](#).

- [28] **ALICE** Collaboration, K. Aamodt *et al.*, “Particle-yield modification in jet-like azimuthal di-hadron correlations in Pb-Pb collisions at $\sqrt{s_{NN}} = 2.76$ TeV,” [*Phys. Rev. Lett.* **108** \(2012\) 092301](#), [arXiv:1110.0121 \[nucl-ex\]](#).
- [29] **ALICE** Collaboration, B. Abelev *et al.*, “Centrality Dependence of Charged Particle Production at Large Transverse Momentum in Pb–Pb Collisions at $\sqrt{s_{NN}} = 2.76$ TeV,” [*Phys. Lett. B* **720** \(2013\) 52–62](#), [arXiv:1208.2711 \[hep-ex\]](#).
- [30] **ALICE** Collaboration, J. Adam *et al.*, “Jet-like correlations with neutral pion triggers in pp and central Pb–Pb collisions at 2.76 TeV,” [*Phys. Lett. B* **763** \(2016\) 238–250](#), [arXiv:1608.07201 \[nucl-ex\]](#).
- [31] **CMS** Collaboration, S. Chatrchyan *et al.*, “Study of high-pT charged particle suppression in PbPb compared to pp collisions at $\sqrt{s_{NN}} = 2.76$ TeV,” [*Eur. Phys. J. C* **72** \(2012\) 1945](#), [arXiv:1202.2554 \[nucl-ex\]](#).
- [32] **CMS** Collaboration, S. Chatrchyan *et al.*, “Centrality dependence of dihadron correlations and azimuthal anisotropy harmonics in PbPb collisions at $\sqrt{s_{NN}} = 2.76$ TeV,” [*Eur. Phys. J. C* **72** \(2012\) 2012](#), [arXiv:1201.3158 \[nucl-ex\]](#).
- [33] N. Armesto, M. Cacciari, T. Hirano, J. L. Nagle, and C. A. Salgado, “Constraint fitting of experimental data with a jet quenching model embedded in a hydrodynamical bulk medium,” [*J. Phys. G* **37** \(2010\) 025104](#), [arXiv:0907.0667 \[hep-ph\]](#).
- [34] **JET** Collaboration, K. M. Burke *et al.*, “Extracting the jet transport coefficient from jet quenching in high-energy heavy-ion collisions,” [*Phys. Rev. C* **90** no. 1, \(2014\) 014909](#), [arXiv:1312.5003 \[nucl-th\]](#).
- [35] **JETSCAPE** Collaboration, S. Cao *et al.*, “Determining the jet transport coefficient \hat{q} from inclusive hadron suppression measurements using Bayesian parameter estimation,” [*Phys. Rev. C* **104** no. 2, \(2021\) 024905](#), [arXiv:2102.11337 \[nucl-th\]](#).
- [36] **ALICE** Collaboration, B. Abelev *et al.*, “Measurement of charged jet suppression in Pb-Pb collisions at $\sqrt{s_{NN}} = 2.76$ TeV,” [*JHEP* **03** \(2014\) 013](#), [arXiv:1311.0633 \[nucl-ex\]](#).

- [37] **ALICE** Collaboration, J. Adam *et al.*, “Measurement of jet suppression in central Pb-Pb collisions at $\sqrt{s_{NN}} = 2.76$ TeV,” [*Phys. Lett. B* **746** \(2015\) 1–14](#), [arXiv:1502.01689 \[nucl-ex\]](#).
- [38] **ATLAS** Collaboration, G. Aad *et al.*, “Measurements of the Nuclear Modification Factor for Jets in Pb+Pb Collisions at $\sqrt{s_{NN}} = 2.76$ TeV with the ATLAS Detector,” [*Phys. Rev. Lett.* **114** no. 7, \(2015\) 072302](#), [arXiv:1411.2357 \[hep-ex\]](#).
- [39] **CMS** Collaboration, V. Khachatryan *et al.*, “Measurement of inclusive jet cross sections in *pp* and PbPb collisions at $\sqrt{s_{NN}} = 2.76$ TeV,” [*Phys. Rev. C* **96** no. 1, \(2017\) 015202](#), [arXiv:1609.05383 \[nucl-ex\]](#).
- [40] **ALICE** Collaboration, J. Adam *et al.*, “Measurement of jet quenching with semi-inclusive hadron-jet distributions in central Pb-Pb collisions at $\sqrt{s_{NN}} = 2.76$ TeV,” [*JHEP* **09** \(2015\) 170](#), [arXiv:1506.03984 \[nucl-ex\]](#).
- [41] **ATLAS** Collaboration, G. Aad *et al.*, “Observation of a Centrality-Dependent Dijet Asymmetry in Lead-Lead Collisions at $\sqrt{s_{NN}} = 2.77$ TeV with the ATLAS Detector at the LHC,” [*Phys. Rev. Lett.* **105** \(2010\) 252303](#), [arXiv:1011.6182 \[hep-ex\]](#).
- [42] **CMS** Collaboration, S. Chatrchyan *et al.*, “Jet momentum dependence of jet quenching in PbPb collisions at $\sqrt{s_{NN}} = 2.76$ TeV,” [*Phys. Lett. B* **712** \(2012\) 176–197](#), [arXiv:1202.5022 \[nucl-ex\]](#).
- [43] **CMS** Collaboration, S. Chatrchyan *et al.*, “Studies of jet quenching using isolated-photon+jet correlations in PbPb and *pp* collisions at $\sqrt{s_{NN}} = 2.76$ TeV,” [*Phys. Lett. B* **718** \(2013\) 773–794](#), [arXiv:1205.0206 \[nucl-ex\]](#).
- [44] **CMS** Collaboration, A. M. Sirunyan *et al.*, “Observation of Medium-Induced Modifications of Jet Fragmentation in Pb-Pb Collisions at $\sqrt{s_{NN}} = 5.02$ TeV Using Isolated Photon-Tagged Jets,” [*Phys. Rev. Lett.* **121** no. 24, \(2018\) 242301](#), [arXiv:1801.04895 \[hep-ex\]](#).

- [45] **ALICE** Collaboration, S. Acharya *et al.*, “First measurement of jet mass in Pb–Pb and p–Pb collisions at the LHC,” [*Phys. Lett. B* **776** \(2018\) 249–264](#), [arXiv:1702.00804 \[nucl-ex\]](#).
- [46] **ALICE** Collaboration, S. Acharya *et al.*, “Exploration of jet substructure using iterative declustering in pp and Pb–Pb collisions at LHC energies,” [*Phys. Lett. B* **802** \(2020\) 135227](#), [arXiv:1905.02512 \[nucl-ex\]](#).
- [47] **CMS** Collaboration, A. M. Sirunyan *et al.*, “Measurement of the Splitting Function in pp and Pb-Pb Collisions at $\sqrt{s_{NN}} = 5.02$ TeV,” [*Phys. Rev. Lett.* **120** no. 14, \(2018\) 142302](#), [arXiv:1708.09429 \[nucl-ex\]](#).
- [48] **STAR** Collaboration, L. Adamczyk *et al.*, “Dijet imbalance measurements in $Au + Au$ and pp collisions at $\sqrt{s_{NN}} = 200$ GeV at STAR,” [*Phys. Rev. Lett.* **119** no. 6, \(2017\) 062301](#), [arXiv:1609.03878 \[nucl-ex\]](#).
- [49] **STAR** Collaboration, L. Adamczyk *et al.*, “Measurements of jet quenching with semi-inclusive hadron+jet distributions in Au+Au collisions at $\sqrt{s_{NN}} = 200$ GeV,” [*Phys. Rev. C* **96** no. 2, \(2017\) 024905](#), [arXiv:1702.01108 \[nucl-ex\]](#).
- [50] **STAR** Collaboration, J. Adam *et al.*, “Measurement of inclusive charged-particle jet production in Au + Au collisions at $\sqrt{s_{NN}} = 200$ GeV,” [*Phys. Rev. C* **102** no. 5, \(2020\) 054913](#), [arXiv:2006.00582 \[nucl-ex\]](#).
- [51] G. David, “Direct real photons in relativistic heavy ion collisions,” [*Rept. Prog. Phys.* **83** no. 4, \(2020\) 046301](#), [arXiv:1907.08893 \[nucl-ex\]](#).
- [52] X.-N. Wang, Z. Huang, and I. Sarcevic, “Jet quenching in the opposite direction of a tagged photon in high-energy heavy ion collisions,” [*Phys. Rev. Lett.* **77** \(1996\) 231–234](#), [arXiv:hep-ph/9605213 \[hep-ph\]](#).
- [53] W. Dai, I. Vitev, and B.-W. Zhang, “Momentum imbalance of isolated photon-tagged jet production at RHIC and LHC,” [*Phys. Rev. Lett.* **110** no. 14, \(2013\) 142001](#), [arXiv:1207.5177 \[hep-ph\]](#).

- [54] **CMS** Collaboration, A. M. Sirunyan *et al.*, “Study of jet quenching with isolated-photon+jet correlations in PbPb and pp collisions at $\sqrt{s_{NN}} = 5.02$ TeV,” [Phys. Lett. B **785** \(2018\) 14–39](#), [arXiv:1711.09738 \[nucl-ex\]](#).
- [55] **ATLAS** Collaboration, M. Aaboud *et al.*, “Measurement of photon–jet transverse momentum correlations in 5.02 TeV Pb + Pb and pp collisions with ATLAS,” [Phys. Lett. B **789** \(2019\) 167–190](#), [arXiv:1809.07280 \[nucl-ex\]](#).
- [56] **ALICE** Collaboration, S. Acharya *et al.*, “Constraints on jet quenching in p-Pb collisions at $\sqrt{s_{NN}} = 5.02$ TeV measured by the event-activity dependence of semi-inclusive hadron-jet distributions,” [Phys. Lett. B **783** \(2018\) 95–113](#), [arXiv:1712.05603 \[nucl-ex\]](#).
- [57] R. Baier, “Jet quenching,” [Nucl. Phys. A **715** \(2003\) 209–218](#), [arXiv:hep-ph/0209038](#).
- [58] **STAR** Collaboration, L. Adamczyk *et al.*, “Jet-like Correlations with Direct-Photon and Neutral-Pion Triggers at $\sqrt{s_{NN}} = 200$ GeV,” [Phys. Lett. B **760** \(2016\) 689–696](#), [arXiv:1604.01117 \[nucl-ex\]](#).
- [59] **STAR** Collaboration, “Measurement of in-medium jet modification using direct photon+jet and π^0 +jet correlations in $p + p$ and central Au+Au collisions at $\sqrt{s_{NN}} = 200$ GeV,” [arXiv:2309.00156 \[nucl-ex\]](#).
- [60] **STAR** Collaboration, B. I. Abelev *et al.*, “Studying Parton Energy Loss in Heavy-Ion Collisions via Direct-Photon and Charged-Particle Azimuthal Correlations,” [Phys. Rev. C **82** \(2010\) 034909](#), [arXiv:0912.1871 \[nucl-ex\]](#).
- [61] M. Cacciari, G. P. Salam, and G. Soyez, “The anti- k_t jet clustering algorithm,” [JHEP **04** \(2008\) 063](#), [arXiv:0802.1189 \[hep-ph\]](#).
- [62] **STAR** Collaboration, K. H. Ackermann *et al.*, “STAR detector overview,” [Nucl. Instrum. Meth. A **499** \(2003\) 624–632](#).
- [63] **STAR** Collaboration, M. Beddo *et al.*, “The STAR barrel electromagnetic calorimeter,” [Nucl. Instrum. Meth. A **499** \(2003\) 725–739](#).

- [64] M. Anderson *et al.*, “The Star time projection chamber: A Unique tool for studying high multiplicity events at RHIC,” *Nucl. Instrum. Meth. A* **499** (2003) 659–678, [arXiv:nucl-ex/0301015 \[nucl-ex\]](#).
- [65] **STAR** Collaboration, M. S. Abdallah *et al.*, “Differential measurements of jet substructure and partonic energy loss in Au+Au collisions at $\sqrt{s_{NN}} = 200$ GeV,” *Phys. Rev. C* **105** no. 4, (2022) 044906, [arXiv:2109.09793 \[nucl-ex\]](#).
- [66] R. Brun, F. Bruyant, M. Maire, A. C. McPherson, and P. Zancarini, *GEANT 3: user’s guide Geant 3.10, Geant 3.11; rev. version.* CERN, Geneva, 1987. <https://cds.cern.ch/record/1119728>.
- [67] T. Sjostrand, S. Mrenna, and P. Z. Skands, “PYTHIA 6.4 Physics and Manual,” *JHEP* **05** (2006) 026, [arXiv:hep-ph/0603175](#).
- [68] P. Z. Skands, “Tuning Monte Carlo Generators: The Perugia Tunes,” *Phys. Rev. D* **82** (2010) 074018, [arXiv:1005.3457 \[hep-ph\]](#).
- [69] **STAR** Collaboration, J. Adam *et al.*, “Longitudinal double-spin asymmetry for inclusive jet and dijet production in pp collisions at $\sqrt{s} = 510$ GeV,” *Phys. Rev. D* **100** no. 5, (2019) 052005, [arXiv:1906.02740 \[hep-ex\]](#).
- [70] T. Sjostrand, S. Mrenna, and P. Z. Skands, “A Brief Introduction to PYTHIA 8.1,” *Comput. Phys. Commun.* **178** (2008) 852–867, [arXiv:0710.3820 \[hep-ph\]](#).
- [71]
- [72] N.-B. Chang and G.-Y. Qin, “Full jet evolution in quark-gluon plasma and nuclear modification of jet production and jet shape in Pb+Pb collisions at 2.76A TeV at the CERN Large Hadron Collider,” *Phys. Rev. C* **94** no. 2, (2016) 024902, [arXiv:1603.01920 \[hep-ph\]](#).
- [73] H. Song, S. A. Bass, and U. Heinz, “Viscous QCD matter in a hybrid hydrodynamic+Boltzmann approach,” *Phys. Rev. C* **83** (2011) 024912, [arXiv:1012.0555 \[nucl-th\]](#).
- [74] T. Luo, S. Cao, Y. He, and X.-N. Wang, “Multiple jets and γ -jet correlation in high-energy heavy-ion collisions,” *Phys. Lett. B* **782** (2018) 707–716, [arXiv:1803.06785 \[hep-ph\]](#).

- [75] L.-G. Pang, Y. Hatta, X.-N. Wang, and B.-W. Xiao, “Analytical and numerical Gubser solutions of the second-order hydrodynamics,” [Phys. Rev. D **91** no. 7, \(2015\) 074027](#), [arXiv:1411.7767 \[hep-ph\]](#).
- [76] Z.-W. Lin, C. M. Ko, B.-A. Li, B. Zhang, and S. Pal, “A Multi-phase transport model for relativistic heavy ion collisions,” [Phys. Rev. C **72** \(2005\) 064901](#), [arXiv:nucl-th/0411110](#).
- [77] W. Zhao, W. Ke, W. Chen, T. Luo, and X.-N. Wang, “From Hydrodynamics to Jet Quenching, Coalescence, and Hadron Cascade: A Coupled Approach to Solving the RAA \otimes v2 Puzzle,” [Phys. Rev. Lett. **128** no. 2, \(2022\) 022302](#), [arXiv:2103.14657 \[hep-ph\]](#).
- [78] W. Chen, S. Cao, T. Luo, L.-G. Pang, and X.-N. Wang, “Effects of jet-induced medium excitation in γ -hadron correlation in A+A collisions,” [Phys. Lett. B **777** \(2018\) 86–90](#), [arXiv:1704.03648 \[nucl-th\]](#).
- [79] Z.-B. Kang, I. Vitev, and H. Xing, “Vector-boson-tagged jet production in heavy ion collisions at energies available at the CERN Large Hadron Collider,” [Phys. Rev. C **96** no. 1, \(2017\) 014912](#), [arXiv:1702.07276 \[hep-ph\]](#).
- [80] J. Casalderrey-Solana, D. C. Gulhan, J. G. Milhano, D. Pablos, and K. Rajagopal, “A Hybrid Strong/Weak Coupling Approach to Jet Quenching,” [JHEP **10** \(2014\) 019](#), [arXiv:1405.3864 \[hep-ph\]](#). [Erratum: JHEP 09, 175 (2015)].
- [81] J. Casalderrey-Solana, Z. Hulcher, G. Milhano, D. Pablos, and K. Rajagopal, “Simultaneous description of hadron and jet suppression in heavy-ion collisions,” [Phys. Rev. C **99** no. 5, \(2019\) 051901](#), [arXiv:1808.07386 \[hep-ph\]](#).
- [82] **STAR** Collaboration, J. Adam et al., “Measurement of inclusive charged-particle jet production in Au + Au collisions at $\sqrt{s_{NN}}=200$ GeV,” [Phys. Rev. C **102** no. 5, \(2020\) 054913](#), [arXiv:2006.00582 \[nucl-ex\]](#).
- [83] **PHENIX** Collaboration, A. Adare et al., “High p_T direct photon and π^0 triggered azimuthal jet correlations and measurement of k_T for

- isolated direct photons in $p + p$ collisions at $\sqrt{s} = 200$ GeV,” [Phys. Rev. D **82** \(2010\) 072001](#), [arXiv:1006.1347 \[hep-ex\]](#).
- [84] H. Zhang, J. F. Owens, E. Wang, and X.-N. Wang, “Dihadron tomography of high-energy nuclear collisions in NLO pQCD,” [Phys. Rev. Lett. **98** \(2007\) 212301](#), [arXiv:nucl-th/0701045](#).
- [85] T. Renk, “Biased showers: A common conceptual framework for the interpretation of high- p_T observables in heavy-ion collisions,” [Phys. Rev. C **88** no. 5, \(2013\) 054902](#), [arXiv:1212.0646 \[hep-ph\]](#).
- [86] S. A. Bass, C. Gale, A. Majumder, C. Nonaka, G.-Y. Qin, T. Renk, and J. Ruppert, “Systematic Comparison of Jet Energy-Loss Schemes in a realistic hydrodynamic medium,” [Phys. Rev. C **79** \(2009\) 024901](#), [arXiv:0808.0908 \[nucl-th\]](#).
- [87] **PHENIX** Collaboration, A. Adare *et al.*, “Systematic Study of Azimuthal Anisotropy in Cu+Cu and Au+Au Collisions at $\sqrt{s_{NN}} = 62.4$ and 200 GeV,” [Phys. Rev. C **92** no. 3, \(2015\) 034913](#), [arXiv:1412.1043 \[nucl-ex\]](#).
- [88] M. Cacciari and G. P. Salam, “Pileup subtraction using jet areas,” [Phys. Lett. B **659** \(2008\) 119–126](#), [arXiv:0707.1378 \[hep-ph\]](#).
- [89] **ALICE** Collaboration, B. Abelev *et al.*, “Measurement of the inclusive differential jet cross section in pp collisions at $\sqrt{s} = 2.76$ TeV,” [Phys. Lett. B **722** \(2013\) 262–272](#), [arXiv:1301.3475 \[nucl-ex\]](#).
- [90] **CMS** Collaboration, S. Chatrchyan *et al.*, “Measurement of the Ratio of Inclusive Jet Cross Sections using the Anti- k_T Algorithm with Radius Parameters $R=0.5$ and 0.7 in pp Collisions at $\sqrt{s} = 7$ TeV,” [Phys. Rev. D **90** no. 7, \(2014\) 072006](#), [arXiv:1406.0324 \[hep-ex\]](#).
- [91] **ALICE** Collaboration, S. Acharya *et al.*, “Measurements of inclusive jet spectra in pp and central Pb-Pb collisions at $\sqrt{s_{NN}} = 5.02$ TeV,” [Phys. Rev. C **101** no. 3, \(2020\) 034911](#), [arXiv:1909.09718 \[nucl-ex\]](#).

- [92] M. Dasgupta, F. A. Dreyer, G. P. Salam, and G. Soyez, “Inclusive jet spectrum for small-radius jets,” [*JHEP* **06** \(2016\) 057](#), [arXiv:1602.01110 \[hep-ph\]](#).
- [93] M. Cacciari, G. P. Salam, and G. Soyez, “The Catchment Area of Jets,” [*JHEP* **04** \(2008\) 005](#), [arXiv:0802.1188 \[hep-ph\]](#).
- [94] **PHENIX** Collaboration, S. S. Adler et al., “Common suppression pattern of eta and pi0 mesons at high transverse momentum in Au+Au collisions at $\sqrt{s_{NN}} = 200\text{GeV}$,” [*Phys. Rev. Lett.* **96** \(2006\) 202301](#), [arXiv:nucl-ex/0601037](#).
- [95] **PHENIX** Collaboration, A. Adare et al., “Azimuthal anisotropy of π^0 and η mesons in Au+Au collisions at $\sqrt{s_{NN}} = 200\text{ GeV}$,” [*Phys. Rev. C* **88** no. 6, \(2013\) 064910](#), [arXiv:1309.4437 \[nucl-ex\]](#).
- [96] **PHENIX** Collaboration, S. Afanasiev et al., “Measurement of Direct Photons in Au+Au Collisions at $\sqrt{s_{NN}} = 200\text{ GeV}$,” [*Phys. Rev. Lett.* **109** \(2012\) 152302](#), [arXiv:1205.5759 \[nucl-ex\]](#).
- [97] **STAR** Collaboration, B. I. Abelev et al., “Systematic Measurements of Identified Particle Spectra in pp, d+Au and Au+Au Collisions from STAR,” [*Phys. Rev. C* **79** \(2009\) 034909](#), [arXiv:0808.2041 \[nucl-ex\]](#).
- [98] A. Hocker and V. Kartvelishvili, “SVD approach to data unfolding,” [*Nucl. Instrum. Meth. A* **372** \(1996\) 469–481](#), [arXiv:hep-ph/9509307 \[hep-ph\]](#).
- [99] G. D’Agostini, “A Multidimensional unfolding method based on Bayes’ theorem,” [*Nucl. Instrum. Meth. A* **362** \(1995\) 487–498](#).
- [100] <http://hepunix.rl.ac.uk/~adye/software/unfold/RooUnfold.html>.
- [101] Bähr, M. and Gieseke, S. and Gigg, M. A. and Grellscheid, D. and Hamilton, K. and Latunde-Dada, O. and Plätzer, S. and Richardson, P. and Seymour, M. H. and Sherstnev, A. and Webber, B. R., “Herwig++ physics and manual,” [*Eur. Phys. J. C* **58** \(2008\) 639](#), [arXiv:0803.0883 \[hep-ph\]](#).

- [102] **ALICE** Collaboration, S. Acharya *et al.*, “Measurement of charged jet cross section in pp collisions at $\sqrt{s} = 5.02$ TeV,” [Phys. Rev. D](#) **100** no. 9, (2019) 092004, [arXiv:1905.02536 \[nucl-ex\]](#).
- [103] J. Casalderrey-Solana, G. Milhano, D. Pablos, and K. Rajagopal, “Modification of Jet Substructure in Heavy Ion Collisions as a Probe of the Resolution Length of Quark-Gluon Plasma,” [JHEP](#) **01** (2020) 044, [arXiv:1907.11248 \[hep-ph\]](#).